1D, 2D and 3D Monte Carlo ambient noise tomography using a dense passive seismic array installed on the North Sea seabed

1D, 2D and 3D Monte Carlo ambient noise tomography using a dense passive seismic array installed on the North Sea seabed

Xin Zhang[1], Fredrik Hansteen[2], Andrew Curtis[1,3]and Sjoerd de Ridder[4]

[1]School of Geosciences, University of Edinburgh, Edinburgh, United Kingdom
[2]Equinor ASA, Bergen, Norway
[3]Department of Earth Sciences, ETH Zürich, Switzerland
[4]School of Earth and Environment, University of Leeds, United Kingdom

Key Points:

- We observe two Scholte wave modes in ambient noise cross-correlations and separate them using a dispersion compensation method.
- We applied Eikonal tomography to obtain phase velocity maps for both the fundamental mode and the first higher mode.
- We compared 1D, 2D and 3D Monte Carlo to invert dispersion data for shear velocity and show that the 3D method gives most accurate results.

Corresponding author: Xin Zhang, x.zhang2@ed.ac.uk

Abstract

In a variety of geoscientific applications we require 3D maps of properties of the Earth's interior, and the corresponding map of uncertainties to assess their reliability. On the seabed it is common to use Scholte wave dispersion data to infer these maps using inversion-based imaging theory. Previously we introduced a 3D fully nonlinear Monte Carlo tomography method that inverts for shear velocities directly from frequency-dependent travel time measurements, and which improves accuracy of the results and better estimates uncertainties. Here for the first time we apply that method to real data and compare it to two of those previous methods. We cross correlated 6.5 hours of ambient noise data recorded on a dense seismic array over Grane, North Sea, and observed two Scholte wave modes. For each mode, phase velocity maps are estimated using Eikonal tomography, which are in turn used to study the shear-wave velocity structure of the subsurface. We applied three nonlinear inversion methods to the Grane data: standard 1D depth inversions, a 2D joint inversion along a vertical cross-section, and a fully 3D inversion. We compare the shear-velocity and uncertainty structures estimated along the same 2D cross-section. Thus we show that the standard 1D inversion method causes errors in the results due to independence of those 1D inversions, whereas the 2D and 3D inversions improve results by accounting for lateral spatial correlations. The 3D inversion bypasses the initial seabed Eikonal tomography step, and therefore avoids the errors it introduces into subsequent 1D and 2D inversions.

1 Introduction

Geoscientists often need to image or monitor the subsurface in order to understand the properties and processes of the Earth's interior. Seismic tomography is a technique which has been used widely to produce three-dimensional models of the properties of the Earth. In order to interpret the imaging results appropriately, and in particular to avoid over-interpretation, it is often desirable to estimate uncertainties in such models.

Seismic surface waves propagate along interfaces in the Earth across which seismic properties change abruptly (Rayleigh and Love surface waves propogate along the Earth's surface, i.e. the interface between solid and air, whereas Scholte waves propogate along the seabed at the interface between liquid and solid), and oscillate over depth ranges that depend on frequency (Aki & Richards, 1980). This in turn makes surface waves dispersive – different frequencies travel at different speeds, and these speeds are sensitive

to different parts of the Earth. By measuring the wave speeds this dispersion property can therefore be used to study the subsurface of the Earth by tomographic imaging on global (Trampert & Woodhouse, 1995; N. Shapiro & Ritzwoller, 2002; Meier et al., 2007a, 2007b; Ferreira et al., 2010; Ekström, 2011) and regional scales (Zielhuis & Nolet, 1994; Curtis et al., 1998; Simons et al., 2002; Y. Yang et al., 2007; Lin et al., 2008; Zigone et al., 2015).

In the above studies, surface waves were generated by earthquakes, which inevitably limits the resolvability of models in regions of sparse coverage due to the inhomogeneous distribution of seismic sources and stations. The introduction of ambient noise interferometry has greatly increased the size and coverage of our surface wave datasets by turning receivers into virtual (imagined) sources. It has been shown theoretically that Green's functions between different receiver pairs can be retrieved by cross correlations of ambient noise data recorded at the receivers (Campillo & Paul, 2003; Wapenaar, 2004; van Manen et al., 2005, 2006; Wapenaar & Fokkema, 2006; Curtis et al., 2006). Surface waves contained in the Green functions can be extracted and used to study subsurface structure (N. M. Shapiro & Campillo, 2004). This method has been used widely to study the regional scale structure of crust and uppermost mantle (N. M. Shapiro et al., 2005; Yao et al., 2006; Lin et al., 2007, 2009; Y. Yang et al., 2007; Yao & Van Der Hilst, 2009; Bensen et al., 2009; Behr et al., 2010; Nicolson et al., 2012, 2014) and the near surface uppermost crustal structure (de Ridder & Dellinger, 2011; de Ridder & Biondi, 2013; Mordret, Landès, et al., 2013; Mordret, Shapiro, et al., 2013; Mordret, Landès, et al., 2014; de Ridder et al., 2014, 2015; Allmark et al., 2018).

In most of the above studies only the fundamental mode surface wave is used due to the fact that higher modes are often so low in amplitude as to be invisible in the data. However, in surface waves generated by earthquakes it has been shown that higher modes can be observed (Gabriels et al., 1987; Park, Miller, & Xia, 1999; Park, Miller, Xia, Hunter, & Harris, 1999) and can be used to further constrain the subsurface structure (Gabriels et al., 1987; Jan van Heijst & Woodhouse, 1999; Xia et al., 2000, 2003). Mordret, Shapiro, and Singh (2014) also observed higher modes in the cross correlations of ambient noise data recorded by ocean bottom cable (OBC) sensors over the Valhall oil field, but since this energy was much weaker than the fundamental mode, these higher modes were ignored. However, in other cases the energy of higher modes can be comparable to the fundamental mode and may cause errors in inferred fundamental mode phase or group ve-

81 locities due to the fact that the modes are mixed together (Xia et al., 2003). Therefore,
82 it is important to correctly identify and separate the different modes.

83 If multiple source-receiver distances are available, higher modes can often be sep-
84 arated from fundamental modes by frequency-wavenumber (F-K) analysis (Gabriels et
85 al., 1987). However, this process assumes that speeds of each frequency are the same for
86 all source-receiver pairs. In order to perform phase or group velocity tomography, we of-
87 ten need accurate phase/group velocity measurements from each mode for each source-
88 receiver pair independently. This means that individual modes need to be separated at
89 each receiver. This can be done by band-pass filtering if the modes occupy different fre-
90 quency bands (Crampin & Båth, 1965), but unfortunately this is not always the case.
91 Other methods based on adaptive wavelet transformations (Kritski et al., 2006; Kuttig
92 et al., 2006) or mode-branch stripping (van Heijst & Woodhouse, 1997) have been pro-
93 posed to quantify the energy of individual modes and to separate them, but those meth-
94 ods risk destroying the phase of individual modes, and thus introducing errors in the phase
95 velocity picks. In this study we therefore used a method based on dispersion compen-
96 sation (Wilcox, 2003; Xu et al., 2012) or equivalently on time reversal (Fink, 1992; Al-
97 leyne et al., 1993; Ing & Fink, 1998). In this method, an individual mode in a disper-
98 sive wave is compressed to a short-duration pulse in the time domain by adjusting the
99 phase to undo the dispersion so that each mode can be separated easily from the oth-
100 ers e.g., by using a time-windowing function. The method has been used successfully to
101 separate Lamb modes in ultrasonic waves (Xu et al., 2012), but has not previously been
102 applied to seismic surface waves.

103 Seismic surface wave inversion problems are often solved using a 2-step scheme of
104 first inverting for two-dimensional (2D) geographical maps of surface wave phase or group
105 velocity and then inverting for the 3D spatial velocity structure using 1D inversions for
106 structure over depth beneath each geographical location (Nakanishi & Anderson, 1983;
107 Trampert & Woodhouse, 1995; Ritzwoller et al., 2002; Snoke & Sambridge, 2002; Bodin
108 & Sambridge, 2009; Bodin et al., 2012; Galetti et al., 2017). The 2D tomographic prob-
109 lem in the first step is usually solved by a linearized procedure by minimizing the data
110 misfit while applying some regularization (Trampert & Woodhouse, 1995; Ritzwoller et
111 al., 2002). However, the regularization is often chosen by ad hoc means (often trial and
112 error), and it can suppress valuable information (Zhdanov, 2002). It has also been shown
113 to be difficult to quantify meaningful uncertainties from linearized ambient noise tomog-

raphy (N. Shapiro & Ritzwoller, 2002; Bensen et al., 2009; Yao & Van Der Hilst, 2009; Weaver et al., 2011; Nicolson et al., 2012, 2014). As a result the 1D depth inversions in the second step can be affected by biased 2D velocity and uncertainty estimation (Young et al., 2013).

To resolve these issues nonlinear inversion methods based on the Markov chain Monte Carlo (McMC) sampling algorithm have been introduced to seismic tomography (Mosegaard & Tarantola, 1995). McMC is a class of methods which generate samples from a target probability density (Metropolis & Ulam, 1949; Hastings, 1970; Mosegaard & Tarantola, 1995; Sivia, 1996; Malinverno et al., 2000; Malinverno, 2002; Malinverno & Briggs, 2004). In seismic tomography, a generalised McMC method called the *reversible jump* algorithm (Green, 1995; Green & Hastie, 2009) is often used; this allows a trans-dimensional inversion to be carried out, which means that the dimensionality of the parameter space (the number of model parameters) can vary in the inversion (Bodin & Sambridge, 2009; Hawkins & Sambridge, 2015; Piana Agostinetti et al., 2015; Burdick & Lekić, 2017; Galetti et al., 2017; Galetti & Curtis, 2018). In these methods, a class of model parametrization is dynamically adapted to both the prior information and the data. The method has been used to estimate phase and group velocity maps of the crustal structure (Bodin & Sambridge, 2009; Zulfakriza et al., 2014; Galetti et al., 2015; Zheng et al., 2017) and to carry out the second depth-inversion step to obtain 3D shear wave velocity structures of the crust and uppermost mantle (Bodin et al., 2012; Shen et al., 2012, 2013; Young et al., 2013; Galetti et al., 2017).

However, Zhang et al. (2018) showed that due to the independence of the many 1D inversions in the second step and possible phase or group velocity errors introduced in the first step, the 2-step method causes biases in estimated 3D shear-wave velocity models no matter whether linearized or McMC methods are used. They proposed an alternative 3D Monte Carlo method that directly inverts frequency-dependent phase or group traveltime measurements in one step, and showed via synthetic tests that the method improves accuracy of the velocity model estimation and produces more intuitively reasonable uncertainties than the traditional 2-step method. A similar idea has also been used with a linearized inversion method (Fang et al., 2015). In this study we apply the 3D Monte Carlo method to study the near surface structure of the Grane field and compare the results to those generated using previous methods.

The Grane oil field is situated in the North Sea, about 185 km west of the city of Haugesund, Norway with a water depth of 127m (Figure 1) and contains heavy crude oil found in turbidite sandstone from the Tertiary period (Pragt et al., 2012). It was first discovered by Norsk Hydro in 1991 and is currently operated by Equinor ASA. It started production in 2003, which is estimated to last for 25 years. The field is composed of one main reservoir and a few other segments at a depth of 1,700 m. A permanent monitoring system has been deployed in the field, which contains 3458 four-component sensors (Z-vertical, N-north, E-east component and H-hydrophone). This records seismic data from the field continuously (Thompson et al., 2015) and thus provides the possibility to use ambient noise tomography to monitor the reservoir.

In the following we first present the ambient noise data and compute their cross correlations to obtain Scholte waves in section 2. In section 3 we briefly describe the dispersion compensation method and use it to separate the different Scholte wave modes. In section 4 we determine phase velocity maps for both the fundamental mode and the first overtone using Eikonal tomography. In section 5 we first review the standard 2-step method and the new 3D method, then apply them to estimate the shear-wave velocity structure over the Grane field. For the 2-step inversion, the phase velocity maps in section 3 are used as data. To further understand the limitation of independent 1D inversions, we also performed a 2D inversion using a 2D parameterization of a 2D cross-section using the same data as in the 1D depth inversions. We then compare all results across the 2D section. We conclude that the 3D Monte Carlo inversion method produces more realistic results, and achieves this with comparable computation cost compared to the standard 2-step Monte Carlo method.

2 Ambient noise interferometry at Grane field

2.1 Noise data recorded by the permanent monitoring system at Grane field

Figure 1 shows the locations of all 3458 sensors over the Grane field, each of which records samples at 500 Hz. The depth of the sea floor is around 127 m, becoming slightly shallower in the northeast (120 m). The sensors are organized along linear cables and consequently have inline and crossline spacings of approximately 50 m and 300 m respectively. This permanent and continuously recording array provides the potential to use

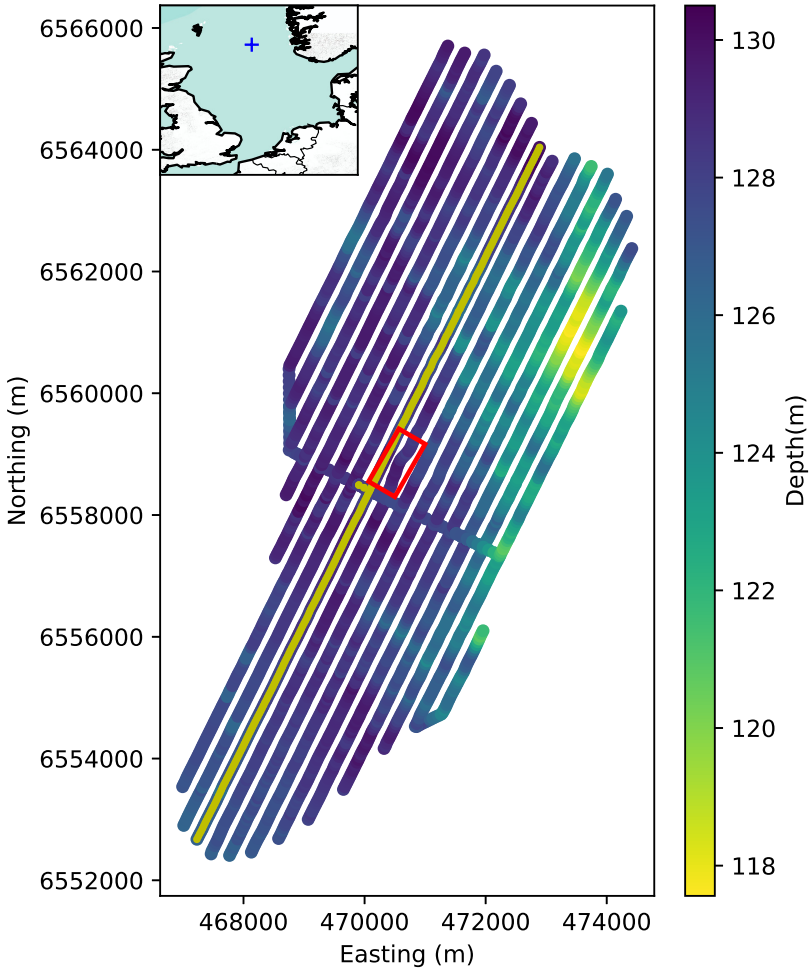

Figure 1. The distribution of receivers at the Grane field coloured according to their depths below sea level. The red box shows the location of the platform and the yellow line shows a receiver line used in the text. The blue plus in the inset map indicates the location of Grane field.

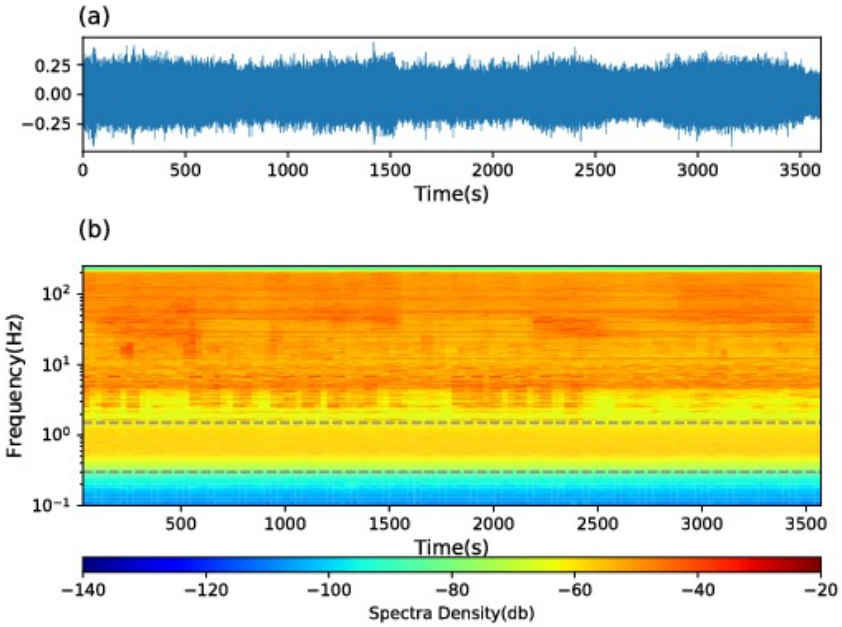

Figure 2. **(a)** An example of one-hour of vertical component data recorded by one of the geophones at Grane field; and **(b)** the corresponding spectrogram. The gray dashed lines bound the frequency range used for cross correlations.

passive seismic interferometry for daily monitoring of the field. In this study, we therefore analysed only 6 hours and 36 minutes of continuous data extracted from recordings in November 2014.

We analysed spectrograms of one-hour intervals of vertical component data extracted from those 6.5 hours of data. Figure 2a shows an example of one such dataset from one receiver. Figure 2b shows the spectrogram of energy across frequency as a function of time computed using 1 minute windows with 50% overlap between windows. The spectrogram is cut off below 0.3 Hz due to the roll-off in receiver sensitivity. The typical frequency response of the receivers is from 3 Hz to 15 KHz. However, it has been shown that lower frequency data can still be used for ambient noise studies (de Ridder & Dellinger, 2011; Mordret, Landès, et al., 2013, 2014). For example, between 0.3 Hz and 1.5 Hz the data are dominated by the tail of the secondary microseismic peak (Webb, 1998) and can be used to estimate Scholte waves from noise cross correlations. Above 1.5 Hz, field-operation noise sources and active seismic sources dominate the data. While it is also possible to obtain useful information about the subsurface using high frequency data (Mordret, Landès, et al., 2013), in this study we focus on the frequency band between 0.3 Hz and 1.5 Hz to obtain Scholte waves and use them to study the near surface structure.

The Scholte waves obtained from noise cross correlations can be biased in the case of an inhomogeneous distribution of noise sources (Wapenaar, 2004; Curtis & Halliday, 2010). Therefore we used the beamforming technique (Cole, 1995; Rost & Thomas, 2002) to characterize the noise distribution of Grane field. The recordings were first band-filtered into a narrow bands (e.g. 0.4-0.6 Hz) to avoid possible blurring of the beamforming results caused by velocity dispersion. The data were then transformed to $\tau - p$ domain by slant stacking (Yilmaz, 2001). Here we carried out beamforming analysis using half-hour segments for all receivers together. Figure 3 shows results for two frequency bands: 0.4-0.6 Hz and 0.6-0.8 Hz. Both results show two circles with different phase velocities, which are associated with different Scholte waves modes. The fundamental mode has a phase velocity of $\sim$580 m/s at the lower band (0.4-0.6 Hz) and a phase velocity of $\sim$520 m/s at the higher band (0.6-0.8 Hz) while the corresponding phase velocity of the first overtone is $\sim$910 m/s and $\sim$830 m/s respectively in each band. Note that the energy of either side of the 0.6-0.8 Hz result is spatial aliasing due to the cross-line sparsity of receivers (Yilmaz, 2001). Although there is residual inhomogeneity, for example, at the lower frequency band the energy in the west is slightly higher than in the east, in both cases

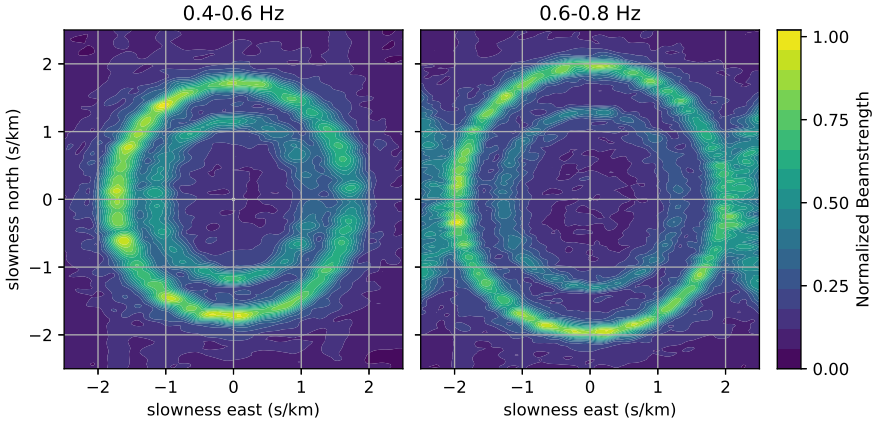

Figure 3. The beamforming results of two narrow frequency bands: 0.4-0.6 Hz (left) and 0.6-0.8 Hz (right) calculated using half-hour data segments.

the noise sources are nearly omnidirectional for both modes, which implies that we have sufficiently equidistributed noise sources for noise-based interferometry and tomography.

2.2 Cross-correlations of ambient noise

Seismic ambient noise interferometry refers to the construction of Green's functions from virtual sources by noise cross correlations (Campillo & Paul, 2003; Wapenaar, 2004; Curtis et al., 2006). The data are first bandpass-filtered to 0.35-1.50 Hz using a frequency domain taper, and down-sampled to 5 Hz sampling rate. Spectral-whitening is then applied to create data with a uniform amplitude spectrum. This process is carried out using half-hour recording segments with a 50% overlap. Finally the data from every station pair are cross correlated segment by segment and results are stacked over the 6.5 hour interval. We did not remove instrument responses because they are identical for all receivers. In this study, we only obtained cross correlations using vertical (Z) components and hydrophone components (H) to construct Rayleigh-type waves, but it would be possible to construct Love waves using north (N) and east (E) components in future (Mordret, Landès, et al., 2013).

Figure 4a and 4d show virtual shot gathers along a receiver line indicated in Figure 1 (yellow line) constructed using pairs of vertical components and pairs of hydrophone components respectively. At long distances the wave packet spreads out in time due to

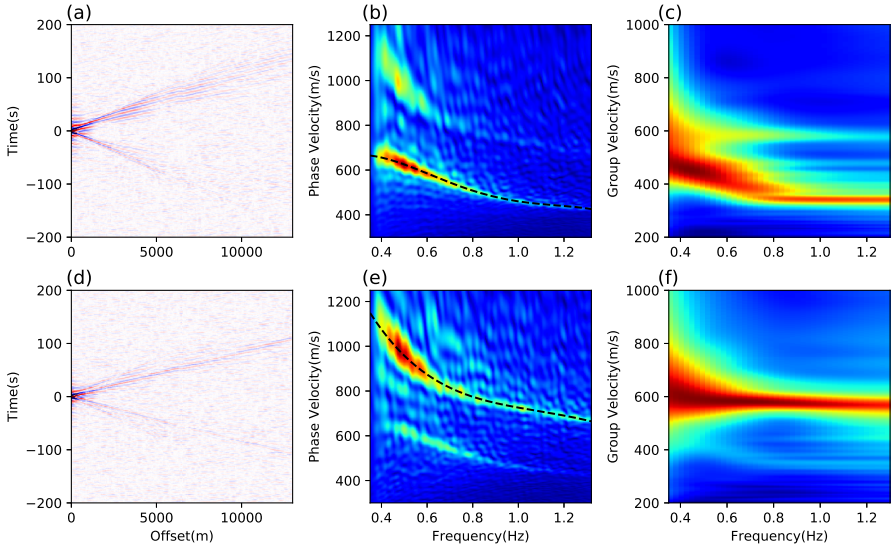

Figure 4. Examples of virtual shot gathers constructed using **(a)** vertical components and **(d)** hydrophone components. The receivers used are shown in Figure 1. **(b)** and **(e)** show the associated phase velocity dispersion analysis using $f - c$ analysis where c is phase velocity, and **(c)** and **(f)** show the associated group velocity dispersion analysis. The black dashed lines indicate the picked phase velocity for the fundamental mode and first overtone.

dispersion. The negative time part has smaller energy than the positive time part, especially at long distances. This may be caused by some residual inhomogeneity in the distribution of noise sources (Figure 3), or some deviation of the noise sources from the ideal sources assumed in theory (mutually uncorrelated point sources).

To analyse the Scholte wave dispersion, we carried out frequency-phase velocity ($f-c$) analysis for the virtual shot gathers in Figure 4a and Figure 4d. The $f-c$ spectrum $U(c,f)$ of gather $u(x,t)$ is computed using:

$$U(c,f) = \iint_{-\infty}^{+\infty} u(x,t) e^{j2\pi f\left(t-\frac{x}{c}\right)}\, dx\, dt \tag{1}$$

where x is distance along the virtual shot gather, t is time, f is frequency, c is phase velocity and $j = \sqrt{-1}$. For this research we used the symmetric part of the correlation results $u(x,t)$ (the mean of the positive and negative time results) after testing that this at least did not appear to be detrimental to results and appeared to increase stability of results. The results (Figure 4b, e) clearly show the two modes that we observed using beamforming analysis (Figure 3). Phase velocity varies from 420 m/s to 660 m/s for

the fundamental mode and from 660 m/s to 1150 m/s for the first overtone. The fundamental mode dominates the signal in the vertical component cross correlations while in the hydrophone components the first overtone dominates, which has been observed before (Savage et al., 2013; Tomar et al., 2018) and has been shown to be related to a few hundred meters of low velocity sediments below the sea floor (Tomar et al., 2018).

We also analyse group velocity dispersion. Group velocities can be obtained by using the traditional frequency-time analysis (FTAN) method (Dziewonski et al., 1969; A. L. Levshin et al., 1972; A. Levshin et al., 1992; Herrin & Goforth, 1977; Russell et al., 1988; Ritzwoller & Levshin, 1998; A. Levshin & Ritzwoller, 2001; Yanovskaya et al., 2012). For each seismic trace, a frequency-time domain envelope image can be obtained by applying a Hilbert transform for a set of narrow frequency bands (e.g. by narrow-band Gaussian filters). To estimate the group velocities for possible different modes, we stacked all those envelope images across the receiver line in Figure 1 to improve signal to noise ratio (Figure 4c, f). Similarly to the phase velocity dispersion analysis, the two modes can be observed in the stacked envelope image. The group velocity of the fundamental mode decreases from 480 m/s to 350 m/s from 0.35 Hz to 0.8 Hz and then shows very little variations after 0.8 Hz. By contrast, the group velocities of the first overtone varies only slightly from 610 m/s to 590 m/s over the frequency range from 0.35 Hz to 1.3 Hz.

3 Mode separation

Although it is often the case that only one mode dominates the signal in a wave (the energy of the first overtone is usually lower than the fundamental mode in vertical component recordings - Figure 4b, c), energy from other modes will still cause bias in the phase or group velocity of each seismic trace (e.g., Xia et al., 2003). For example, at low frequencies (< 0.5 Hz) the group velocities of the two modes are very close and probably cannot be identified individually easily, which may cause biases in phase or group velocity picking (see below). This could produce errors in subsequent tomography results. Therefore, in order to obtain accurate phase or group velocity picks for each trace and for each mode, we first need to separate the modes.

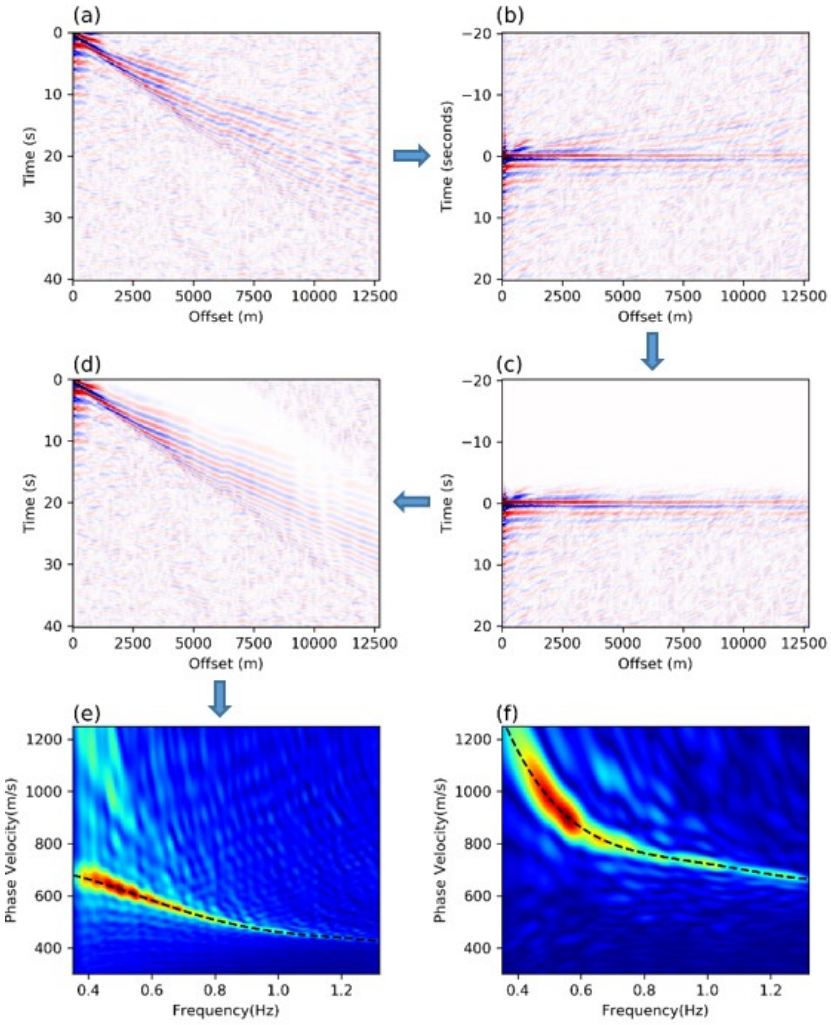

Figure 5. An example of the mode separation procedure. **(a)** The virtual shot gather before mode separation (obtained from Figure 4a by adding positive and negative times). **(b)** Flattened virtual shot gather obtained by dispersion compensation. **(c)** Filtered flattened virtual shot gather. **(d)** Virtual shot gather after mode separation. **(e)** Phase velocity dispersion analysis after mode separation. **(f)** Phase velocity dispersion analysis after using a similar method to instead isolate the first overtone. Arrows show the order of processing steps. Black dashed lines show the associated phase velocity dispersion curves.

3.1 Method

We use a dispersion compensation method to separate different modes (Xu et al., 2012). For seismic surface waves we assume that two modes S and A are excited by a broadband source excitation $F(w)$, and that the phase velocity of the modes are constant across the area. In the frequency domain the recorded surface wave at distance x_0 can then be expressed as

$$G_{SA}(w) = [Amp_S H_S(w) + Amp_A H_A(w)]F(w) \tag{2}$$

where $H_S(w) = exp(-jk_S(w)x_0)$ and $H_A(w) = exp(-jk_A(w)x_0)$, $k_S(w)$ and $k_A(w)$ are dispersion relations of mode S and mode A respectively, and Amp_S and Amp_A are their amplitudes. If $k_S(w)$ and $k_A(w)$ are known, the process of dispersion can be reversed by back-propagation or dispersion compensation. For example, multiplying equation (2) by $H_S^{-1}(w) = exp(jk_S(w)x_0)$ gives

$$\begin{aligned} G^*_{SA}(w) &= H_S^{-1}(w)G_{SA}(w) \\ &= Amp_S F(w) + Amp_A H_S^{-1}(w)H_A(w)F(w) \end{aligned} \tag{3}$$

where $G^*_{SA}(w)$ is the surface wave after dispersion compensation. The first term $Amp_S F(w)$ has no dispersion (propagation) term so will be focused to a short-duration pulse $f(t)$ in time domain at zero time, which can be extracted using a window function. The second term is the residual term from mode A which is still dispersive. After separating mode S from the other waves, it can be propagated back to distance x_0 by multiplying the extracted signal by $H_S(w)$. The result then can be used to estimate more accurate phase or group velocities for mode S, and a similar operation can be used to extract mode A.

In practice, the dispersion relations $k_S(w)$ or $k_A(w)$ are usually not constant across the area of study. However, they often vary smoothly across space at least locally. So equation (3) can still be used for approximate dispersion compensation. Alternatively, one can integrate along estimated source to receiver ray path to estimate the correct dispersion to each receiver if an approximate estimate of the phase velocity map is known. This dispersion estimate can then be used for $k_S(w)$ or $k_A(w)$ as appropriate. In this study, we simply applied equation (3) using estimates of dispersion relations (picked from an initial frequency-wavenumber analysis such as that shown in Figure 4).

3.2 Application to Grane field

We used the method above to separate different modes across Grane field. The data were first back-propagated to time zero in the frequency domain using equation (3) using the dispersion relation of the fundamental mode picked using $f-c$ analysis (black dashed line in Figure 4b), and then transformed back to the time domain. Figure 5b shows the results after dispersion compensation for the symmetric part of the virtual shot gather in Figure 4a. The symmetric gather is shown in Figure 5a. After dispersion compensation, the fundamental mode focuses to an impulsive signal at zero time so that energy in the shot gather becomes flat. Those waves that exist at negative time and are not flat are higher modes since higher modes generally travel faster than the fundamental mode. They can be muted using a time-domain window function (Figure 5c). Figure 5d shows the shot gather after windowing out the higher modes and transforming back to the original propagation time. Figure 5e shows the dispersion image obtained from $f-c$ analysis using the virtual shot gather after mode separation (Figure 5d). At most frequencies (0.5 - 1.3 Hz) the energy of the first overtone disappears, indicating that the higher modes have been removed successfully. However, at low frequencies (0.35-0.5 Hz) some energy from the first overtone remains. This can be explained by the fact that at these frequencies (0.35 - 0.5 Hz) the group velocities of the two modes are very close (Figure 4c) which leads to the modes overlapping even after back-propagation to time zero.

Similarly to the separation of the fundamental mode, we apply the method to obtain waves containing higher modes only. Since the first overtone dominates the signal in cross correlations of hydrophone components (Figure 4e, f), we used those cross correlations to retrieve the first overtone. The phase velocity dispersion curve picked from the result of $f-c$ analysis (Figure 4e) is used to carry out the phase correction. The fundamental mode is then windowed out using a window function and consequently waves containing only the first overtone are obtained (Figure 5f). Finally, after mode separation we obtain Scholte waves that contain only the fundamental mode or the first overtone, which can be used to pick accurate phase or group velocities for each mode.

4 Phase velocity tomography

4.1 Method

To perform phase or group velocity tomography, we first need to pick phase or group velocities for each cross correlation between each station-pair. There are so many pairs that this process must be automated. Group velocity can be picked using the FTAN method (see description in section 2.2). For phase velocity picking we used an image transformation technique (Yao et al., 2006). First a time-period image ($t - T$) is constructed by applying a set of narrow-band filters to the data. This can be transformed to a velocity-period image ($c - T$) by transforming time to phase velocity, for the moment assuming a straight-ray path between each station pair (Figure 6). Finally the phase velocity dispersion curve can easily be identified and automatically picked on the $c-T$ image. The 2π ambiguity of phase velocity measurements can be resolved using our initial estimate of the average phase velocity dispersion curve obtained using $f-c$ analysis (black line in Figure 4b; white line in Figure 6).

To improve the quality of dispersion data, we applied a series of data selection criteria. A minimum signal to noise ratio (SNR) of 5 is used for the fundamental mode and 2.5 is used for the first overtone. The SNR is calculated using the spectrum of the signals of interest and the spectrum of an interval of noise extracted from the end of the virtual source records. Due to the far-field approximation that is implicit in the ambient noise interferometry method, those station-pairs whose distances are smaller than twice the wavelength at any frequency are discarded (Yao et al., 2006; Lin et al., 2009). Considering the possible biases introduced by mode separation in the frequency range of 0.35 - 0.5 Hz (2 - 2.85 s period) – see Figure 5e – in phase velocity tomography we only used phase velocities at frequencies larger than 0.5 Hz ($<$ 2 s period).

We picked phase velocities and group velocities for each station-pair, which can then be used to perform phase or group velocity tomography. Group velocity tomography can be conducted using straight-ray tomography since the data accuracy usually does not merit a more sophisticated approach and since an accurate phase velocity map is not available in order to trace rays to allow group velocity to be calculated along rays (de Ridder & Dellinger, 2011; Mordret, Landès, et al., 2013; Allmark et al., 2018). However, since that the phase velocity measurements are more accurate than group velocities (Yao et al., 2006) and since Eikonal tomography is more efficient and more accurate than straight-

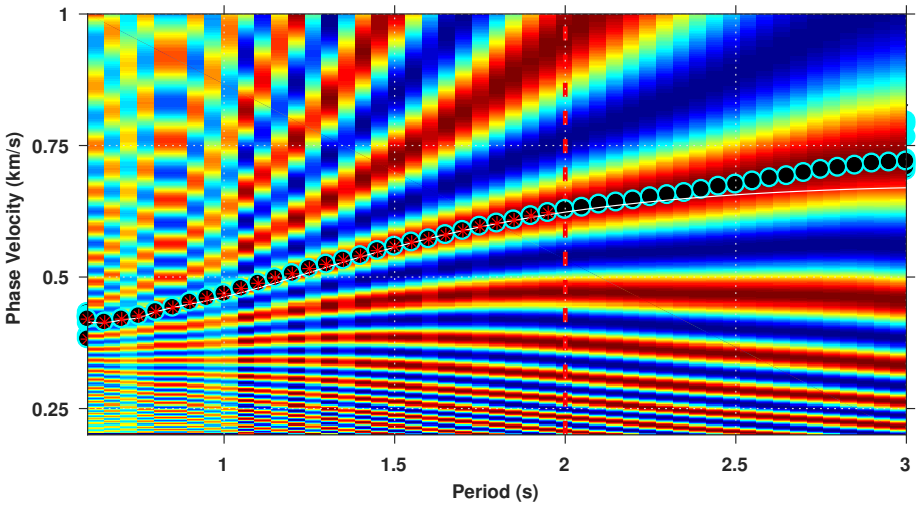

Figure 6. An example of the $c - T$ image used to pick phase velocities. The dashed black line shows the maximum period allowed by the far-field approximation (the offset must be larger than twice the wavelength). The black dots denote the picked phase velocity for the whole period range and the red stars show phase velocities that are actually used. The white line shows the phase velocity dispersion curve obtained using $f - c$ analysis.

ray tomography (Lin et al., 2009), we performed phase velocity tomography using the Eikonal method as we now describe.

In a smoothly heterogeneous medium, the propagation of a single surface wave mode can be expressed using the Eikonal equation (Aki & Richards, 1980; Biondi, 1992; Wielandt, 1993; Shearer, 1999):

$$\frac{1}{c_i(w,\mathbf{r})^2} = |\nabla\tau_i(w,\mathbf{r})|^2 - \frac{\Delta A_i(w,\mathbf{r})}{A_i(w,\mathbf{r})w^2} \tag{4}$$

where c is the phase velocity, τ is the travel time, A is the spectral amplitude, w is the angular frequency, $\mathbf{r}$ is the location, and subscript i denotes the i^{th} source. If the second term on the right-hand side can be ignored (see discussion in Lin et al. 2009), this equation becomes:

$$\frac{1}{c_i(w,\mathbf{r})} = |\nabla\tau_i(w,\mathbf{r})| \tag{5}$$

In this case the local phase slowness at location $\mathbf{r}$ is simply related to the magnitude of the gradient of the travel time field. Therefore, the local phase velocity can be determined using equation (5) by calculating the gradient of the travel time field from each virtual source (Lin et al., 2009).

In order to determine the gradient of the travel time field, we first interpolate the travel time field to a regular grid (Lin et al., 2009). Here we used the biharmonic spline interpolation to interpolate the field to a $50m \times 50m$ grid (de Ridder & Dellinger, 2011). To better control the quality of the interpolated field, for each location we only use interpolated travel times that are surrounded by four measurements. Due to small SNR at large offsets we discarded measurements whose offsets are greater than 6km.

Finally, the average phase slowness $s_0(x)$ at location x and its standard deviation $\sigma_{s_0}(x)$ can be computed using all virtual sources by

$$s_0(x) = \frac{1}{n}\sum_{i=1}^{n} s_i(x) \tag{6}$$

$$\sigma^2_{s_0}(x) = \frac{1}{n(n-1)}\sum_{i=1}^{n}(s_i(x) - s_0(x))^2 \tag{7}$$

where n is the number of sources and i denotes the i^{th} source. Thereafter the phase velocity c_0 and its uncertainty σ_{c_0} can be determined by:

$$c_0(x) = \frac{1}{s_0(x)} \tag{8}$$

$$\sigma_{c_0}(x) = \frac{1}{s_0(x)^2}\sigma_{s_0(x)} \tag{9}$$

4.2 Results

We applied Eikonal tomography for both the fundamental mode and the first overtone in the period range 0.7 s to 2 s. The final mean phase velocity map and its standard deviation are averaged over the 3458 sources for each period. Figure 7 shows the results of fundamental mode tomography at periods 0.7 s, 1.0 s, 1.3 s and 1.6 s. At short periods ($<$ 1.6 s), there is a clear low velocity anomaly in the middle of the field (location delineated by the blue solid line box in the 1s period map). At the west edge between Y=8 km and Y=10 km, a clear low velocity anomaly exists at 0.7 s which fades out from 1.0 s to 1.3 s. At 0.7 s a low velocity channel connects this low velocity anomaly to the middle low velocity anomaly. However, it disappears at longer periods ($>$ 0.7 s), which indicates that this is probably a very near surface structure. Instead at periods of 1 s and 1.3 s, there is a high velocity channel from middle west to north east (location delineated by white solid line box in the 1s period map) which is interrupted by the low velocity channel at 0.7 s. Next to this high velocity channel there is a parallel low velocity channel (location delineated by the black dashed line box) existing at short periods ($<$ 1.6 s). In the south, a low velocity anomaly also emerges (location delineated

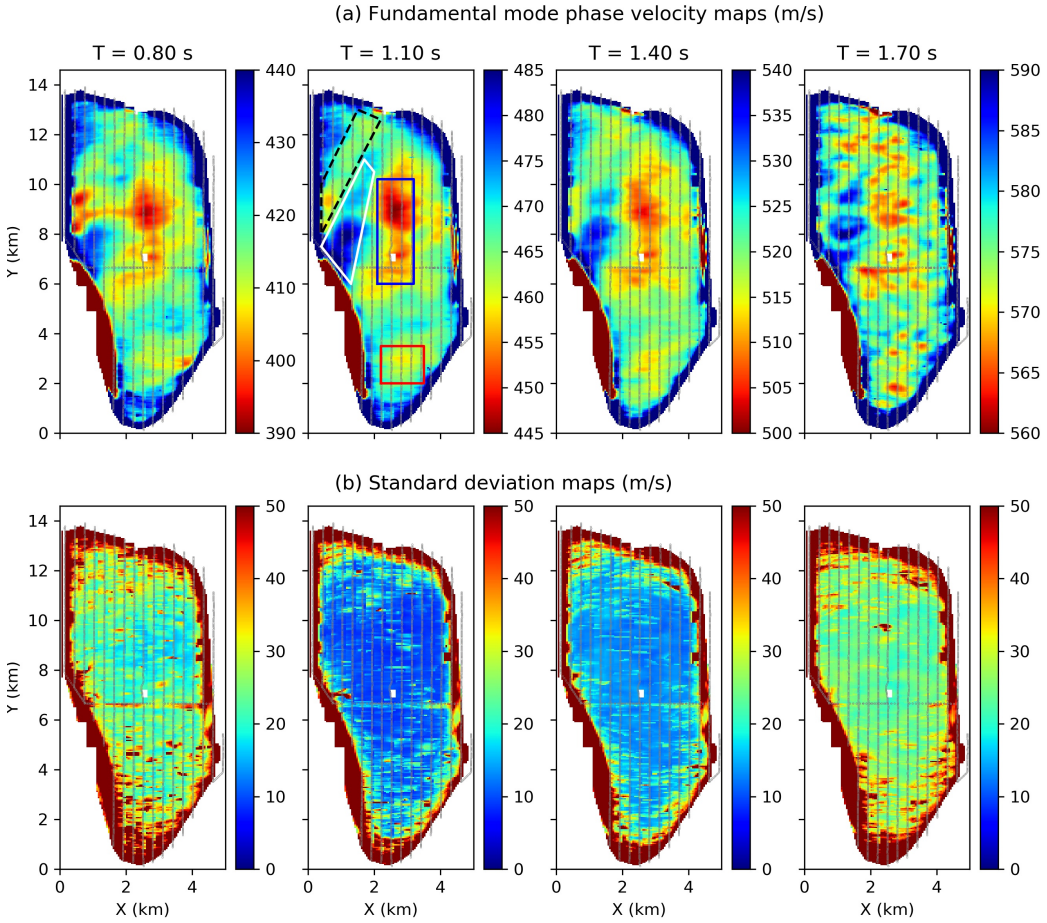

Figure 7. **(a)** Phase velocity maps of the fundamental mode and **(b)** their associated standard deviation maps at periods 0.7s, 1.0s, 1.3s and 1.6s. The boxes show locations of features discussed in the text. Gray lines show the distribution of receivers.

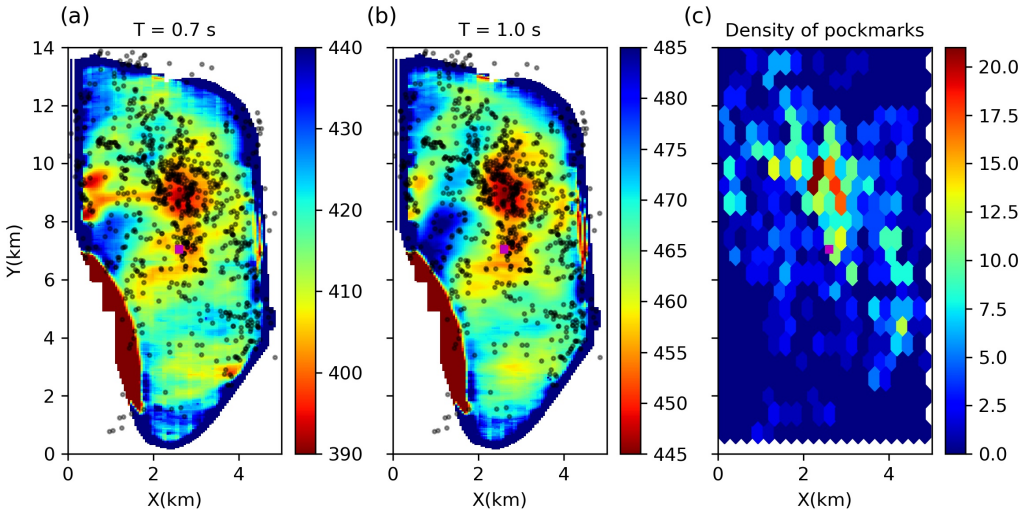

Figure 8. Phase velocity maps at (a) 0.7 s and (b) 1.0 s plotted with pockmarks (black dots). (c) The density of pockmark distribution. The magenta rectangle shows the location of the platform.

by red solid line box). However, at period 1.6 s though there seems to be some degree of similarity in structures with the shorter periods ($<$ 1.6 s), the phase velocity map becomes more complicated. This might due to the poor data quality at longer periods, or may be caused by complex structure at greater depths.

Overall the uncertainties are low at periods of 1.0 s and 1.3 s ($\sim 10m/s$) and are higher at periods of 0.7 s and 1.6 s ($\sim 25m/s$). The high uncertainties at 0.7 s are probably caused by the filtering taper at the lower period side (0.67 s - 0.74 s) while the high uncertainties at 1.6 s probably indicate higher data uncertainties due to lower SNR since phase velocities at longer periods must usually be measured at longer offsets which may also partly explain the complex structure in the mean phase velocity map at 1.6 s. Close to the boundaries all standard deviation maps show very high uncertainties caused by limited data coverage. At the location of the middle low velocity anomaly (blue box), the standard deviation map at 0.7 s shows relatively lower uncertainties; this suggests that the middle low phase velocity anomaly is probably caused by a low velocity structure near to the surface.

To better understand the phase velocity maps, we compared the phase velocity map at 0.7s and 1.0 s with the distribution of pockmarks at the seabed of Grane field (Fig-

ure 8). Pockmarks are craters in the seabed which have been shown to be related to the seepage of fluids (gas or liquids) (Kvenvolden, 1989). Figure 8 shows that there is a dense distribution of pockmarks at the location of the middle low velocity anomaly from the platform to Y=11 km, which suggests that the low velocity anomaly might be caused by near surface fluids. At the west edge, the two low velocity anomalies between Y=8 km and Y=10 km are also consistent with a higher density of pockmark distribution.

Figure 9a shows the mean phase velocity maps of the first overtone at the same periods as for the fundamental mode. We again outline some noticeable features in the phase velocity map at 1 s period. At short periods (< 1.6 s), there is a low velocity anomaly at the west edge (blue line box), with a different shape to that observed in the fundamental mode phase velocity maps. This might suggest that this anomaly is caused by a change in shape with depth since higher mode phase velocities usually have higher sensitivities at greater depths compared to fundamental modes. To the north of this low velocity anomaly there is a low velocity channel at periods of 0.7 s and 1.0 s (red solid line box). At the northern edge, a low velocity channel crosses the field from west to east (black line box). Similarly, this low velocity channel cannot be clearly observed on the fundamental mode phase velocity maps, which indicates that it might be related to deeper structure. In the south of the field there is a similar low velocity anomaly as observed in the fundamental mode phase velocity maps (black dashed line box), which may indicate a consistent low velocity structure from shallow to deeper levels. Overall, at longer periods (i.e. 1.3 s and 1.6 s) the phase velocity maps show very complicated structures as we have seen in the fundamental mode phase velocity map at period of 1.6 s. This may suggest a complicated deeper structure, or may simply be due to the low quality of data at longer periods. Note that the phase velocity maps of the first overtone exhibit much shorter scale structure compared to the fundamental model because of lower data quality of the first overtone. When these phase velocities are used to invert for shear velocities, the shorter scale structure may cause lack of coherence between adjacent 1-D models over depth. To reduce this issue, instead of using Eikonal tomography a regularised inversion might be used to estimate spatially smoother phase velocity maps.

Overall the standard deviation maps of the first overtone show higher uncertainties compared to the fundamental mode (Figure 9b) due to the fact that the SNR of the first overtone is lower than that of the fundamental mode. Similarly to the fundamental mode, higher uncertainties are observed at periods of 0.7 s and 1.6 s ($\sim 100 m/s$) than

at periods of 1 s ($\sim 50m/s$) and 1.3 s ($\sim 80m/s$). The uncertainties are significantly smaller between Y=8 km and Y=10 km at periods of 0.7 s and 1.6 s, showing that this area is well determined, so the low velocity anomaly at this area (blue line box) is well determined. Similarly, there is low uncertainty at the north edge associated with the low velocity channel (black line box) and low uncertainty in the south associated with the low velocity anomaly (black dashed line box). The standard deviation map at 0.7 s shows some higher uncertainty areas ($\sim 160m/s$), e.g., the western edge between Y=10 km and Y=12 km and between Y=6 km and Y= 8 km, which is probably caused by low resolution of those areas. Similarly, there is a high uncertainty area between Y=10 km and Y=12 km at the west edge at period of 1.6 s.

5 Shear-wave velocity inversion

Although these phase velocity maps can be interpreted for useful information about the subsurface, such maps cannot provide good indications of the depths of observed structures since Scholte wave phase velocities are a consequence of the velocity structure over a range of depths. In order to better understand the subsurface structure it is necessary to estimate subsurface shear-velocity structures with depth in a separate inversion. Traditionally, a two-step inversion scheme is used to invert for shear-velocity structures where we use the above phase velocity maps as data and perform 1D depth inversions independently beneath each geographical location. However, Zhang et al. (2018) used synthetic data to show that such a scheme introduces biases in the final 3D shear-velocity structure because each of the depth inversions is conducted independently, whereas in reality they are strongly correlated spatially. Zhang et al. (2018) therefore proposed a fully 3D Monte Carlo inversion method using a 3D parameterization which preserves these correlations.

To further understand the limitations of traditional two-step inversion schemes, in this section we compare results from the two-step method and the 3D method on real data. We use Markov chain Monte Carlo (McMC) to perform both the 1D depth inversions and the 3D inversion. To limit the computational cost, we only carried out 1D depth inversions along a 2D cross-section (the yellow line in Figure 1). In order to study the effects of independent 1D inversions, we also carried out a 2D depth inversion along this cross-section using a 2D parameterization and the phase velocities along the profile on the above maps as data. This inversion is of interest because it uses the phase velocity

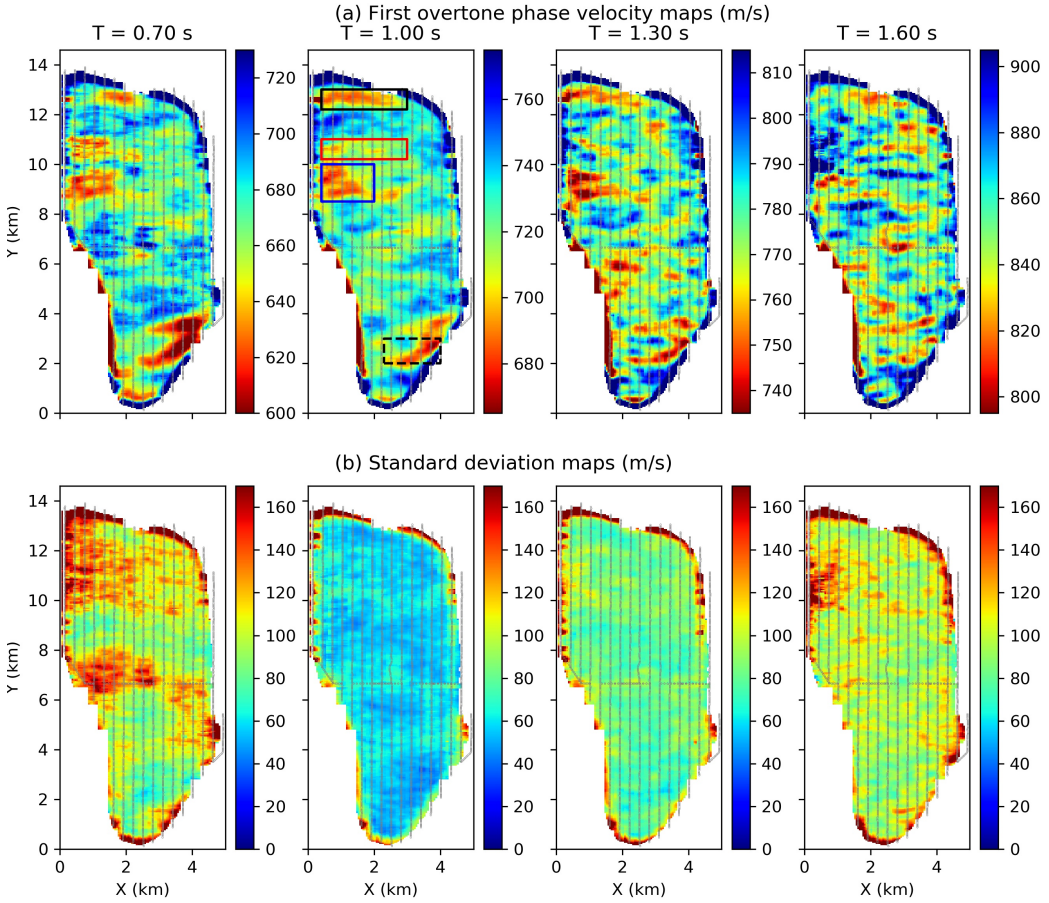

Figure 9. **(a)** Phase velocity maps of the first overtone and **(b)** their standard deviation maps at periods 0.7s, 1.0s, 1.3s and 1.6s. The boxes in the 1 s period map show locations of features discussed in the text. Gray lines show the distribution of receivers.

maps as data similarly to the 1D inversion, but preserves spatial correlations similarly to the 3D method. It would therefore be expected a priori to exhibit intermediate performance compared to the other two methods. In this section, we first describe the two-step methods and the 3D method, and then give an overview of the reversible-jump McMC method and the parallel tempering method (which is used to improve computational efficiency of McMC method). We then apply those methods to the Grane data and compare their results.

5.1 Methods

5.1.1 Parameterization

As in Bodin and Sambridge (2009) and Zhang et al. (2018), we use Voronoi tessellations to parameterize the subsurface. A Voronoi cell is defined by a point (called a site) and its volume that consists of all of the points nearer to this site than to any other. Figure 10 shows examples of Voronoi tessellations in 1D, 2D and 3D. Each cell contains its location and its properties (e.g., P-wave velocity, shear-wave velocity, density, etc.). Note that in 1D the parametrization with Voronoi cells is inferior to the parametrization with a simple partition model since the same velocity model can be obtained using different configuration of Voronoi cells (Green, 1995). However, for comparison purpose in this study we still use a 1D Voronoi parametrization. Since seismic surface waves are primarily sensitive to subsurface shear-wave velocity variations, we only invert for shear-wave velocities. P-wave velocity is linked to the shear-wave velocity via an empirical relation (Castagna et al., 1985):

$$V_p = 1.16V_s + 1.36 \tag{10}$$

and density is computed from the P-wave velocity empirically (Brocher, 2005):

$$\rho = 1.74V_p^{0.25} \tag{11}$$

where V_p and V_s are in km/s, and density ρ is in g/cm^3. Similar to Zhang et al. (2018), within each Voronoi cell the velocity is spatially constant.

The specific choice of Voronoi parametrization makes it easy to implement in 1D, 2D and 3D for comparison. At any point in the model, a velocity profile is a layered model whose phase or group velocity dispersion curve can be computed using many available codes (e.g. Herrmann, 2013) without resorting to approximations. However, while the

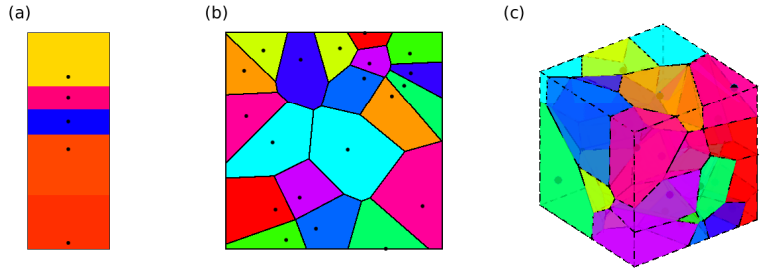

Figure 10. Examples of **(a)** a 1D Voronoi tessellation, **(b)** a 2D Voronoi tessellation and **(c)** a 3D Voronoi tessellation of velocity models. Colours represent seismic velocities in each cell. Black dots are the sites that generated each cell.

Voronoi parametrization is good at recovery of discontinuities, it can introduce difficulties to recover a smooth model (Hawkins et al., 2019). The scale length of Voronoi cells in higher dimensions can cause models to be distorted and some ad-hoc rescaling is generally required (Zhang et al., 2018). It has also been found that Voronoi parametrization can produce multi-modalities in the posterior which makes interpretation of uncertainties difficult. In these cases one could try some other parametrizations, such as wavelets (Hawkins & Sambridge, 2015; Dettmer et al., 2016), Johnson-Mehl tessellation (Belhadj et al., 2018) and Delaunay and Clouth-Tocher parametrization (Hawkins et al., 2019).

5.1.2 2-step inversion

The shear-wave velocity structure is estimated using a 2-step scheme as follows. In the first step a series of 2-D phase or group velocity maps for different frequencies are estimated tomographically using source-to-receiver or inter-receiver arrival times as data; then at each geographical point, the local dispersion curve is used to invert for a 1-D shear velocity profile beneath that point. For the first step, either linearised (Nakanishi & Anderson, 1983; Trampert & Woodhouse, 1995; Ritzwoller et al., 2002; Snoke & Sambridge, 2002; Nicolson et al., 2012, 2014) or non-linearised methods (Bodin & Sambridge, 2009; Bodin et al., 2012; Khan et al., 2013; Young et al., 2013; Rawlinson et al., 2014; Zulfakriza et al., 2014; Saygin et al., 2015; Galetti et al., 2015, 2017; Zheng et al., 2017) can be used

to estimate phase or group velocity maps. In this study, since we have a very dense station network, we used Eikonal tomography to determine phase velocity maps (see above).

For the second step, we use a non-linear McMC method to invert for the 1-D shear velocity profile beneath each point (Bodin et al., 2012; Young et al., 2013; Galetti et al., 2017). Generally those 1D depth inversions are run independently at each geographical location without interaction, as this allows perfect parallelisation of what is a computationally demanding task. We also carried out a 2D depth inversion along the 2D cross-section by using the 2D parameterization described in Figure 10b so as to include lateral spatial correlations in the inversion. The data used for the 2D inversion is the same as those used in the 1D inversions (the local phase velocities from Eikonal tomography). For both the 1D and 2D inversions, we used the same forward modelling method, a modal approximation method (Herrmann, 2013), to calculate the phase velocity dispersion curves from the velocity-versus-depth profiles beneath each geographical point.

5.1.3 Fully 3D inversion

In order to determine a 3D shear-velocity model and to be able to compare the three different methods (1D, 2D and 3D inversions), we also performed a 3D inversion using the 3D McMC method of Zhang et al. (2018). The subsurface is discretized by Voronoi cells (Figure 10c), each of which is defined by the location of its site and its shear-wave velocity. As in Zhang et al. (2018), the forward modelling method is an approximate 2-step method (Ritzwoller & Levshin, 1998; Stevens et al., 2001; Reiter & Rodi, 2008): first a series of phase or group velocity maps at each measurement period are computed by extracting the shear velocity profile with depth beneath each geographical point to what the 1D modal approximation method of Herrmann (2013) is applied to predict group and phase velocities at each period; then for each source-to-receiver or inter-receiver pair, the travel times for each period can be determined by tracing rays through the computed phase velocity map (for which we use the fast marching method – Rawlinson and Sambridge (2004)).

However, as shown in Galetti et al. (2017), modal approximation methods that are usually used (Herrmann, 2013; Saito, 1988) produce unrealistic dispersion curves when applied to relatively unusual velocity-depth models. This is due to the fact that these methods solve the period equation for the minimum phase velocity solution; unfortunately

when the top layer does not have the lowest shear-wave velocity, the dispersion curve with minimum phase velocity is likely to be one of the trapped modes generated by a low velocity layer at depth (Chen, 1993; Wu & Chen, 2016). These trapped modes generally oscillate within the low velocity layer, meaning that they cannot actually be observed on Earth's surface and hence do not correspond to forward model using the recorded data. Therefore, in order to make the modal approximation modelling package that we used (Herrmann, 2013) valid for our inversion, we added a prior constraint on our models – that the smallest shear-wave velocity must be in the top layer. The prior is achieved by rejecting any proposals of violating models in the Markov chain using a large penalty. Note that this choice of prior causes shear velocities at the near surface to prefer small values (see Support information, Figure S1). Considering that this is generally thought to be true for most of the real Earth, we feel that this is an acceptable and pragmatic solution.

5.1.4 Reversible-jump Markov chain Monte Carlo (McMC)

McMC is a class of algorithms that generate a set (or chain) of samples from a target probability density (Sivia, 1996). The Metropolis-Hastings algorithm (Metropolis & Ulam, 1949; Hastings, 1970) is one such algorithm and was introduced to Geophysics over two decades ago (Mosegaard & Tarantola, 1995; Malinverno et al., 2000; Malinverno, 2002; Malinverno & Briggs, 2004). In this study, we use a generalised version of the Metropolis-Hastings algorithm called reversible jump Markov chain Monte Carlo (rj-McMC) (Green, 1995; Green & Hastie, 2009). This algorithm allows a trans-dimensional inversion which means that the number of model parameters can change along the chain. Thus the parameterization of the seismic velocity model can itself be determined by data and prior information, avoiding fixing the parameterisation prior to inversion (Bodin & Sambridge, 2009; Bodin et al., 2012; Young et al., 2013; Galetti et al., 2015, 2017; Hawkins & Sambridge, 2015; Piana Agostinetti et al., 2015; Burdick & Lekić, 2017; Zhang et al., 2018). Note that the specific choice of parametrization (e.g., Voronoi cells) can impose restrictions on models and may affect the final results (Hawkins et al., 2019).

In seismic tomography, the target probability density can be expressed as a Bayesian posterior probability density function (pdf) of the velocity model $\mathbf{m}$ given the observed

data $\mathbf{d}_{obs}$, written $p(\mathbf{m}|\mathbf{d}_{obs})$. According to Bayes' theorem,

$$p(\mathbf{m}|\mathbf{d}_{obs}) = \frac{p(\mathbf{d}_{obs}|\mathbf{m})p(\mathbf{m})}{p(\mathbf{d}_{obs})} \tag{12}$$

where $p(\mathbf{d}_{obs}|\mathbf{m})$ is called the *likelihood* and is the probability of observing the measured data conditional on a certain model $\mathbf{m}$ being true, $p(\mathbf{m})$ describes the prior information about model $\mathbf{m}$ (information that is known independent of data $\mathbf{d}_{obs}$), and $p(\mathbf{d}_{obs})$ is a normalization factor called the *evidence*. We assume a Gaussian data error distribution for our likelihood with the data variance as an additional parameter that is also estimated during the inversion hierarchically (for more information see Malinverno & Briggs, 2004; Bodin et al., 2012; Galetti et al., 2017; Zhang et al., 2018). For the prior pdf we use an uninformative prior – a Uniform distribution with wide bounds on the values of each parameter.

In the rj-McMC algorithm, a new model $\mathbf{m}^{'}$ in the chain is drawn from a proposal distribution $q(\mathbf{m}^{'}|\mathbf{m})$ that depends on the current model $\mathbf{m}$, and is accepted or rejected with a probability $\alpha(\mathbf{m}^{'}|\mathbf{m})$ called the acceptance ratio, given by (Green, 1995)

$$\alpha(\mathbf{m}^{'}|\mathbf{m}) = min[1, \frac{p(\mathbf{m}^{'})}{p(\mathbf{m})} \times \frac{q(\mathbf{m}|\mathbf{m}^{'})}{q(\mathbf{m}^{'}|\mathbf{m})} \times \frac{p(\mathbf{d}_{obs}|\mathbf{m}^{'})}{p(\mathbf{d}_{obs}|\mathbf{m})} \times |\mathbf{J}|] \tag{13}$$

where $\mathbf{J}$ is the Jacobian matrix of the transformation from $\mathbf{m}$ to $\mathbf{m}^{'}$ and is used to account for the volume changes of parameter space during jumps between dimensionalities. In our case, it can be shown that the Jacobian is an identity matrix (Bodin & Sambridge, 2009). Once a new model is generated via the proposal distribution, it is accepted or rejected by generating a random number γ from the uniform distribution on [0, 1] and comparing it with the value of the acceptance ratio α. If $\gamma < \alpha$, the new model is accepted; otherwise, the new model is rejected and the current model is repeated as a new sample in the chain. The form of the acceptance ratio α in equation 13 ensures that the density of samples in the Markov chain converges to the Bayesian posterior probability distribution $p(\mathbf{m}|\mathbf{d}_{obs})$ as the number of samples tends to infinity (Green 1995).

In seismic tomography problems five types of model perturbations are possible: adding a new Voronoi cell, removing a cell, moving a cell, changing the velocities and changing the data noise hyperparameters. Thus, our algorithm can be described as:

1. Draw an initial model randomly from the prior pdf.

2. Generate a new model $\mathbf{m}'$ by randomly choosing one of the five possible perturbation types listed above, and then perturbing the current model according to the proposal probability.
3. Calculate the acceptance ratio α and accept the proposed model to be the new sample with probability α; otherwise use the current model as the new sample.
4. Repeat from (ii).

We use a Gaussian proposal distribution for the fixed-dimensional perturbations of moving a cell, changing velocities and changing data noise hyperparameters (Bodin & Sambridge, 2009; Zhang et al., 2018). For trans-dimensional perturbations (adding or deleting a cell) we choose to use the prior pdf as the proposal probability since that leads to a higher acceptance ratio compared to using a Gaussian distribution (Dosso et al., 2014; Zhang et al., 2018). It is a property of McMC methods that in principle the choice of proposal distribution does not affect the fact that the final distribution of samples tends to the posterior pdf as the number of samples tends to infinity, although Galetti and Curtis (2018) show that in practice improper Gaussian steps can lead to non-convergence of the chain.

To make the ensemble of Markov chains more manageable in size, we only retain every 100th sample of the chain. Monitoring of McMC convergence can be difficult and is always subjective (Green & Hastie, 2009; Bodin & Sambridge, 2009). In this study, we monitored several scalar statistics such as the absolute residual and the number of cells, to diagnose apparent convergence (Bodin & Sambridge, 2009; Hawkins & Sambridge, 2015; Piana Agostinetti et al., 2015; Galetti et al., 2017; Zhang et al., 2018). However, we note that this is still an open problem.

5.1.5 Parallel tempering

Parallel tempering is a technique that mixes information between parallel tempered Markov chains to improve efficiency of McMC methods (Earl & Deem, 2005; Dettmer & Dosso, 2012; Dosso et al., 2012; Sambridge, 2013). First, a set of chains are scaled using different temperatures, such that their target probability can be denoted as:

$$\pi(\mathbf{m}|T_i) = p(\mathbf{m}|\mathbf{d})^{1/T_i}, \tag{14}$$

where T_i is the i^{th} temperature, $p(\mathbf{m}|\mathbf{d})$ is the posterior probability density and $\pi(\mathbf{m}|T_i)$ is called the tempered posterior pdf. Those tempered Markov chains are then run in parallel. Models can be swapped between chains randomly based on an acceptance ratio called detailed balance (Earl & Deem, 2005; Sambridge, 2013):

$$\alpha(i,j) = min\{1, \Big[\frac{p(\mathbf{m}_j|\mathbf{d})}{p(\mathbf{m}_i|\mathbf{d})}\Big]^{1/T_i} \Big[\frac{p(\mathbf{m}_i|\mathbf{d})}{p(\mathbf{m}_j|\mathbf{d})}\Big]^{1/T_j}\}, \tag{15}$$

where $\alpha(i,j)$ is the acceptance ratio of a swap between model $\mathbf{m}_i$ and $\mathbf{m}_j$ at temperature T_i and T_j, respectively. By doing so, one can sample the combined posterior distribution $\pi(\mathbf{m}|T_i), (i = 1, ..., n)$. At higher temperatures the posterior probability density function becomes flatter, which improves the ability of McMC to escape local minima and to explore parameter space more globally. By enabling exchange between different temperatures, the method thus improves the explorative performance of the Markov chain at $T = 1$, which (still) samples our target posterior probability.

The choice of temperature ladder of the parallel chains strongly affects the efficiency of parallel tempering. It has been shown that a power-law temperature schedule is generally more efficient than a uniformly distributed schedule (Calderhead & Girolami, 2009; Sengupta et al., 2015), so here we used a power-law schedule. Given a total of N chains, the temperatures can be distributed as:

$$1/T_i = 1 - \Big(\frac{i}{N}\Big)^p, \tag{16}$$

where T_i is the i^{th} temperature and p is the power coefficient which can be chosen accordingly. To reduce the overhead introduced by synchronization and communication of parallel chains, we only swap models every 50th iteration.

Usually only samples from those chains with $T = 1$ are stored for later inference (Sambridge, 2013; Ray et al., 2017; Galetti & Curtis, 2018). However, for sophisticated problems, parallel tempering often demands a large number of tempered chains to improve the efficiency of McMC methods, which leads to a high computational cost. Those chains with $T > 1$ can also be used for Bayesian inference via an importance resampling scheme (Geyer, 1994; Dosso et al., 2012). Suppose that we have samples from an unnormalized density h and want to calculate an integration with respect to another unnormalized density h_θ. This is important since most of the statistics that we usually wish to calculate (the mean model, variance, etc.) are integrals. Such integrals can be com-

puted by using the importance sampling formula as weighted averages:

$$E_\theta g(X) = \sum_{j=1}^{n} w_\theta(X_j) g(X_j) \tag{17}$$

where θ denotes that the expectation is calculated with respect to probability density h_θ, g is the function of which we want to calculate expectation, and

$$w_\theta(x) = \frac{h_\theta(x)/h(x)}{\sum_{j=1}^{n} h_\theta(X_j)/h(X_j)} \tag{18}$$

Substituting $h_\theta(x)$ with $\pi(\mathbf{m}|T_0)$, and $h(x)$ with $\pi(\mathbf{m}|T_i)$, the weight $w_{T_0}(\mathbf{m})$ can be expressed as:

$$w_{T_0}(\mathbf{m}) = \frac{\pi(\mathbf{m}|T_0)/\pi(\mathbf{m}|T_i)}{\sum_{j=1}^{n} \pi(\mathbf{m}_j|T_0)/\pi(\mathbf{m}_j|T_i)} \tag{19}$$

where $\mathbf{m}_j$ is the j^{th} sample from the chain with $T = T_i$, $T_0 = 1$, and $\pi(\mathbf{m}|T_0)$ is the density in which we are interested. Combining equation (19) with equation (14), w_{T_0} will be:

$$w_{T_0}(\mathbf{m}) = \frac{\pi(\mathbf{m})^{1-\frac{1}{T_i}}}{\sum_{j=1}^{n} \pi(\mathbf{m}_j)^{1-\frac{1}{T_i}}} \tag{20}$$

where $\pi(\mathbf{m}) = p(\mathbf{m}|\mathbf{d})$ is the target posterior at $T = 1$. Using this equation and equation (17), one can calculate any expectations using samples from the tempered chain with $T = T_i$ with respect to the target density $\pi(\mathbf{m})$.

5.2 Application to Grane field

We applied the above suite of methods to the Grane field data to estimate shear-wave velocity structures and compared the results. In this section, we used phase velocity dispersion data of fundamental mode Rayleigh-type Scholte waves to invert for the shear-wave velocity structure. For two-step inversions (the 1D and 2D inversions described above) we extracted those local phase velocities that lie along the top of a 2D cross-section (see Figure 1) from the phase velocity maps. This produces 257 dispersion curves, one for each geographical location (Figure 11). Since the computational cost scales with the minimum of the number of virtual sources and receivers, for the 3D inversion we only used a subset of 36 receivers as virtual sources (Figure 12a), each recorded on all 3458 receivers, and picked phase velocities for each virtual source-to-receiver pair. This generates 41842 dispersion curves which constitutes our 3D inversion dataset. Figure 12b shows a density map of straight ray paths for those picked phase velocities at 1.0 s. Similarly to the above phase velocity tomography, we only used periods from 0.7 s to 2.0 s with a spacing of 0.1 s (Figure 12c).

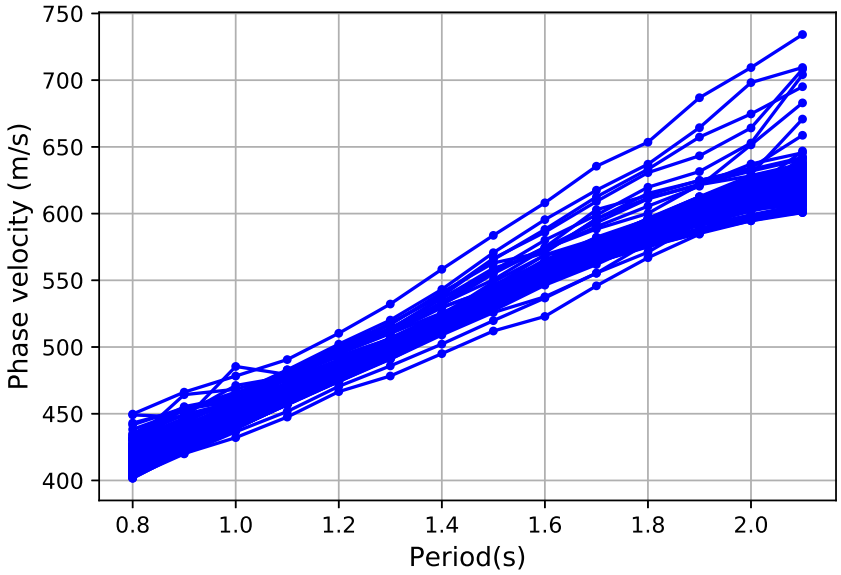

Figure 11. Local phase velocity dispersion curves at points along a 2D cross-section (yellow line in Figure 1) extracted from phase velocity maps. These were used as data for our two-step inversions (1D and 2D inversions).

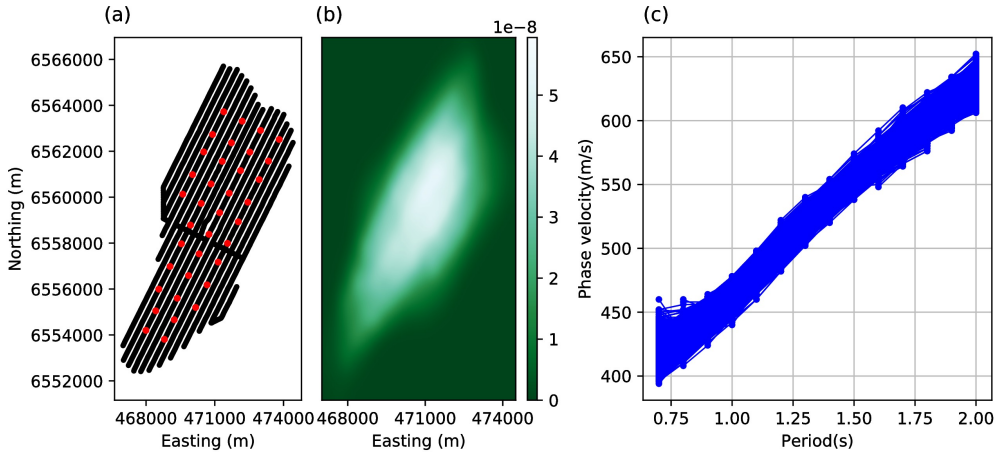

Figure 12. **(a)** Receivers used as virtual sources (red dots) for the 3D inversion. Phase velocity dispersion curves are picked from those virtual sources to all 3458 receivers. **(b)** Density of ray paths of phase velocity at 1.0 s and **(c)** phase velocity (travel time) dispersion curves.

For 1D depth inversions, the prior pdf of the number of layers is chosen to be a discrete uniform distribution between 2 and 20 layers and the prior of shear velocity is set to be a uniform distribution between 200 m/s and 1400 m/s. The noise level of the likelihood is parameterized using a hyperparameter γ which serves as a scaling factor of a prior Gaussian uncertainty that has standard deviation which comes from the results of Eikonal tomography above (Galetti et al., 2017). The prior of this hyperparameter is simply chosen to be a uniform distribution between 0.001 and 1.0. Since the sea floor depth varies smoothly across Grane field, we assumed an averaged water depth of 127 m everywhere. For the proposal distribution we use a Gaussian distribution: the width of the Gaussian for fixed-dimensional steps (velocity change, moving a cell site and hyperparameter change) is chosen by trial and error to ensure the acceptance ratio is between 20 and 50 percent (Hawkins & Sambridge, 2015; Zhang et al., 2018); the width for the trans-dimensional step (birth and death) is selected to produce the maximum possible acceptance ratio. For each inversion at each geographical location we used eight chains, and each chain is run for 3,000,000 iterations with a burn-in period of 1,000,000 during which all samples are ignored for subsequent inference of the posterior pdf. Each chain is thinned by retaining every 100th sample after burn-in, and those samples are used to estimate the posterior pdf's mean and standard deviation.

For the 2D inversion we used a discrete uniform distribution between 100 and 400 as the prior on the number of cells, and the same prior distribution for shear velocity as in 1D inversions. For the noise parameterization we used only one hyperparameter for each period across the section as a scaling factor for uncertainties from Eikonal tomography. Thus we maintain the relative uncertainty structures from Eikonal tomography across the 2D section. The prior for this hyperparamter is chosen to be a uniform distribution between 0.01 and 1. Similarly to above, the proposal distribution for fixed-dimensional steps (velocity change, moving a cell, hyperparameter change) is selected to give an acceptance ratio between 20 and 50 percent. For the trans-dimensional step (birth and death) we used the prior pdf as the proposal distribution (Dosso et al., 2014; Zhang et al., 2018). As shown in Zhang et al. (2018), the high lateral-to-vertical spatial aspect ratio fo the cross-section can affect the efficiency of McMC sampling when using Voronoi cells. Therefore, we applied a scaling factor of 8 for the vertical dimension to reduce the aspect ratio. We used a total of 16 chains for the 2D inversion and collected 4,000,000 samples

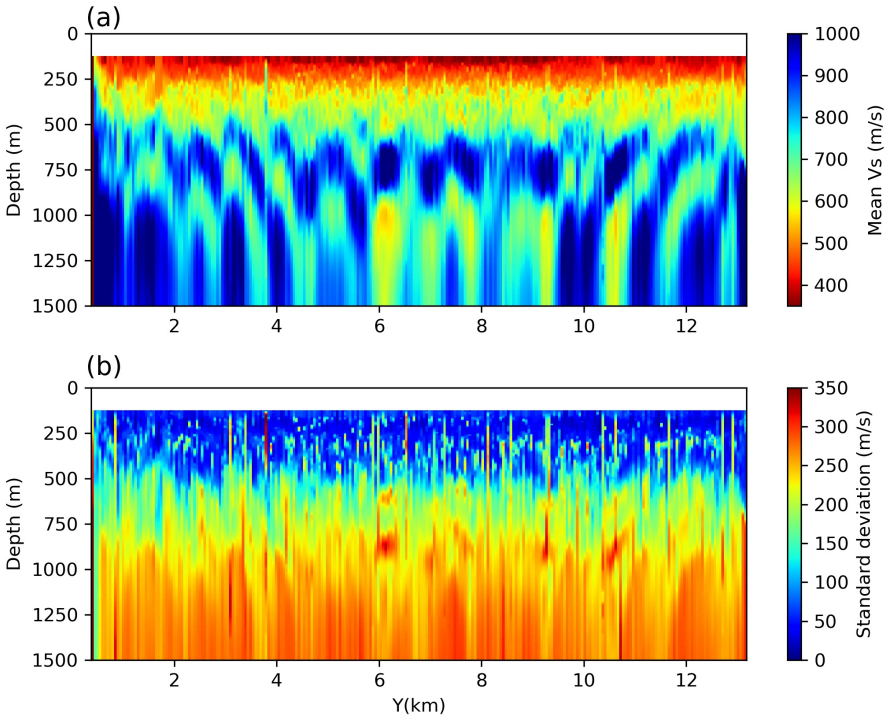

Figure 13. **(a)** Mean and **(b)** standard deviation of shear velocity Vs along the 2D cross-section (see Figure 1) from independent 1D Monte Carlo depth inversions. The white top layer represents the water layer which has zero shear velocity.

from each chain with a burn-in period of 2,000,000. Each chain is thinned by a factor of 100.

For the 3D inversion, the prior of the number of cells is set to be a discrete uniform distribution between 400 and 1500 since the Grane field has a relatively complex structure as indicated by the complex phase velocity maps. We used the same prior for the shear velocity as in 1D and 2D inversions. The noise level is derived from two parameters σ_0 and σ_1 using equation $\sigma = \sigma_0 * traveltime + \sigma_1$ as in Zhang et al. (2018). The prior density of the two noise hyperparameters are set to be a uniform distribution between 0.0001 and 0.02 and a uniform distribution between 0.0 and 0.1, respectively. The proposal distribution for fixed-dimensional steps are chosen in a similar way to those in the 1D and 2D inversions. For trans-dimensional steps the prior is used as the proposal distribution. As in the 2D inversion, the vertical aspect ratio is scaled by 8 to compensate for the high lateral-to-vertical difference in scaling. To improve the efficiency of

3D McMC we applied parallel tempering. A total of 24 chains are used with 16 chains at temperature 1. The temperatures of the other chains are chosen using equation (16) with $p = 3$ and $N = 8$. For each chain we generated 2,700,000 samples with a burn-in period of 1,000,000 and maintained only every 100th sample after burn-in.

5.3 Results of shear velocity tomography

Figure 13 shows the shear-velocity mean and standard deviation from 1D inversions. In the near surface ($<$ 250 m), the model has a relatively low velocity layer ($\sim$ 400 m/s, see Figure 16a). Between 250 m and 600 m the velocity is slightly higher ($\sim$ 650 m/s) and shows complicated structures which are likely caused by the independence of each 1D inversion. This latter effect is also reflected by some laterally sharp discontinuities across the section. Below 600 m the model shows a high velocity layer ($\sim$ 900 m/s) between Y=6 km and Y=9.5 km down to 800 m. At each side (Y $<$ 6 km and Y$>$ 9.5 km), parallel, dipping, alternating high and low velocity anomalies are observed across the section. At the bottom ($>$ 800 m) there exists alternating vertical high and low velocity anomalies. These high and low velocity anomalies are possibly related to similar structures observed in the phase velocity maps at longer periods (Figures 7 and 9). However, due to high uncertainties ($>$ 200 m/s) at greater depths ($>$ 600 m, see Figure 16) , those complicated structures are probably not interpretable. The standard deviation map (Figure 13b) shows that the near surface structure ($<$ 500 m) is apparently well constrained since surface waves are more sensitive to shallower depths (Figure 16a). Note however that there are also lateral discontinuities in the uncertainty map caused by the independence of each 1D inversion; these generally show that the corresponding phase velocity discontinuities are not well resolved (they have very high uncertainty). Note that in this study the phase velocity maps are obtained using Eikonal tomography in which no explicit regularization is imposed. As a result the phase velocity maps show some short-scale structures which may cause some roughness in the shear velocity model estimated by independent 1D inversions. To reduce this issue the conventional regularized tomography may be used to produce smoother phase velocity maps, and consequently to produce a smoother shear velocity model.

For comparison, Figure 14 shows the results from the 2D inversion. Overall the mean velocity model is smoother because of lateral interactions that are included in the 2D parameterization. The near surface structure is generally similar to that from 1D inver-

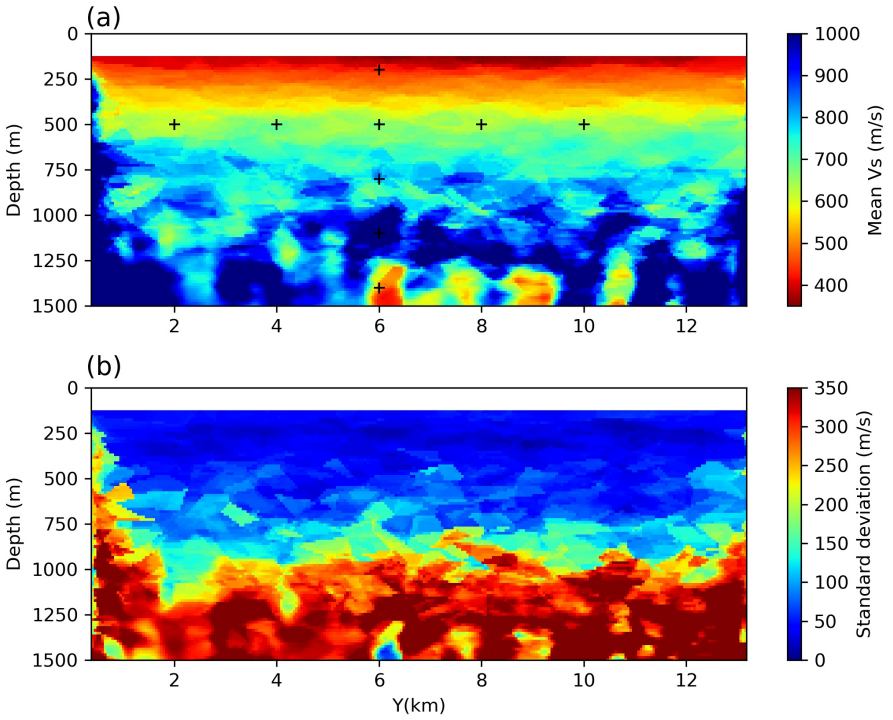

Figure 14. **(a)** Mean and **(b)** standard deviation of shear velocity along the 2D cross-section (see Figure 1) from the 2D Monte Carlo inversions. The white top layer represents the water layer which has zero shear velocity.Black pluses indicate locations of which marginal distributions are shown in Figure S3 in support information.

sions: a low velocity layer at depths < 250 m. However, between 250 m and 600 m, the 2D result shows far smoother structures compared to the discontinuous structures in the 1D result. Below 600 m the two results show very different structures. Instead of the clear high velocity anomalies and dipping structures that appeared between 600 m and 800 m in the 1D result, the 2D result exhibits smoother structures. Below 800 m the structure becomes more complicated and at greater depths (> 1000 m) we also observe some vertical high and low velocity anomalies similar to the 1D results. The standard deviation map shows that uncertainties are relatively small (< 100 m/s) from the surface down to 800 m (Figure 16b), which is significantly deeper than for the 1D inversions (500 m). This is probably because by including lateral spatial correlations, and because the near surface structure is better determined which further improves the resolution at greater depths. Below 800 m we have very high standard deviations (~ 350 m/s) as expected.

Note that in the 2D results, there are artefacts caused by Voronoi cells at greater depths (> 500 m). To evaluate convergence of Markov chains, Figure S2 in the supporting information shows the history of misfits and averaged noise level, and the histogram of number of cells. We also show marginal distributions of shear velocity at points in the cross section (black pluses in Figure 14) in Figure S3. To further study the convergence and the results of the 2D inversion, we conducted another independent inversion with the same number of chains and the same number of samples as in the previous 2D inversion. The results (Figure S4 in the supporting information) show similar results to those in the previous 2D results. We therefore conclude that the 2D Markov chains have almost converged. However, because errors in the phase velocity maps obtained using Eikonal tomography may produce a complex posterior distribution of shear velocity models, it is certainly possible that Markov chains got stuck at local modes. This may be the reason for the Voronoi cell shaped artefacts.

Note that there is a low velocity anomaly with small standard deviations at Y=6 km at the bottom of the cross section, which also exists in the 1D inversion results (Figure 13) and in another 2D inversion result (Figure S4). Therefore the anomaly may be caused by errors in the phase velocity maps which requires a low velocity value at greater depths. Since the bottom layer of models are assumed to be a half-space, these aggregated the resolution of velocity at all greater depths, which explains why the anomaly shows a low standard deviation (this is a common problem for such trans-dimensional depth inversion – see Zhang et al., 2018). Note that smoother velocity and uncertainty

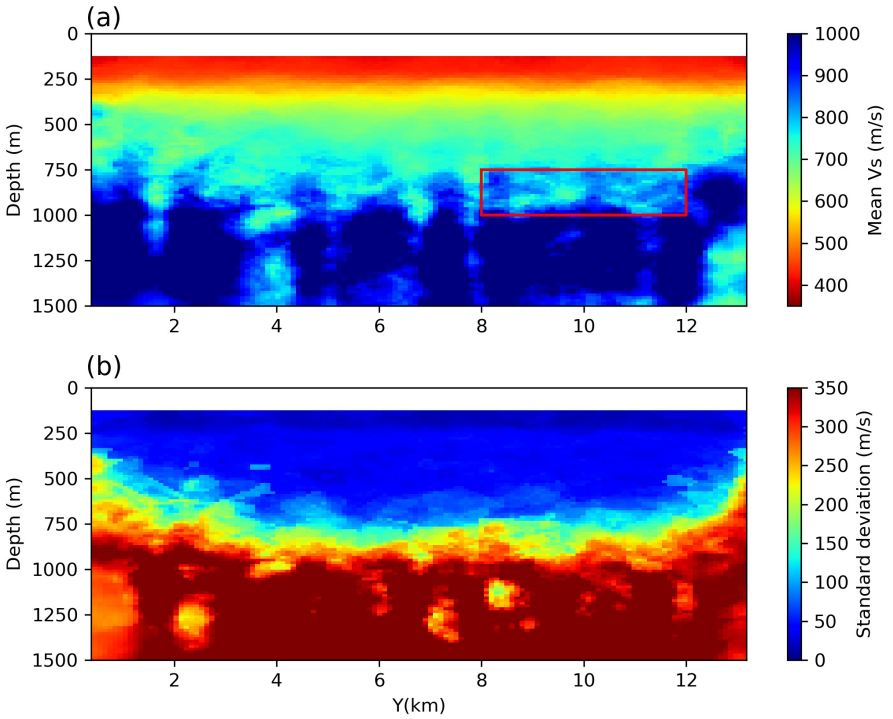

Figure 15. **(a)** Mean and **(b)** standard deviation of shear velocity along the 2D cross-section (see Figure 1) from the 3D Monte Carlo inversion. The white top layer represents the water layer which has zero shear velocity.

models can be obtained by explicitly smoothing the results (Young et al., 2013; Chmiel et al., 2019). For fair comparison of our various models, and to try to avoid ad hoc steps in processing we do not apply any smoothing in this study.

We show the results from the 3D inversion in Figure 15. In the near surface (< 250 m) the structure is very similar to the 2D result, showing a clear low velocity layer (Figure 16c). Between 250 m and 800 m the structure is smoother compared to both the 2D and 1D results, and does not show the high velocity anomalies and dipping structures that exist in the 1D result. Around 800 m there is a possible high velocity layer from Y=8 km to Y=12 km and beneath it there are some isolated low velocity anomalies at around 1000 m depth (red box in Figure 15). At the west (Y< 8 km), the model shows some high and low velocity anomalies between 800 m and 1000 m. Though the structure beneath 1000 m is relatively smooth and shows high velocities (> 900 m/s), there are still some vertical structures similar to those in the 2D and 1D results. This suggests

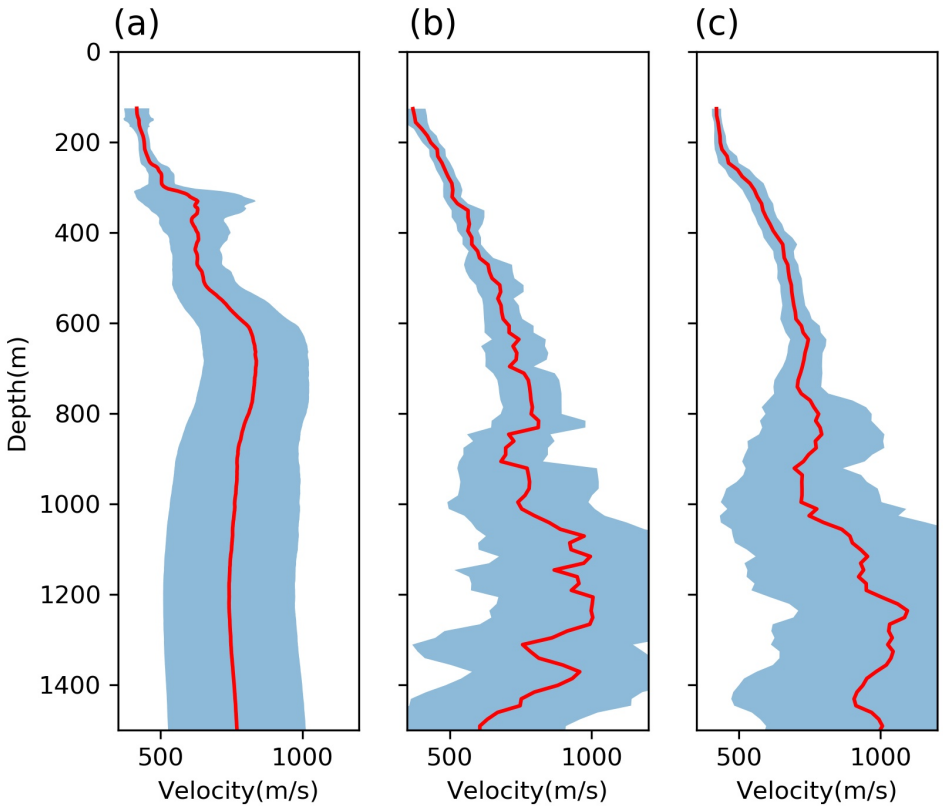

Figure 16. 1D marginal mean (red line) and standard deviation (blue area) at the middle (Y=6.7 km) of the 2D cross-section (see Figure 1) obtained using **(a)** the 1D Monte Carlo inversion, **(b)** the 2D Monte Carlo inversion and **(c)** the 3D Monte Carlo inversion.

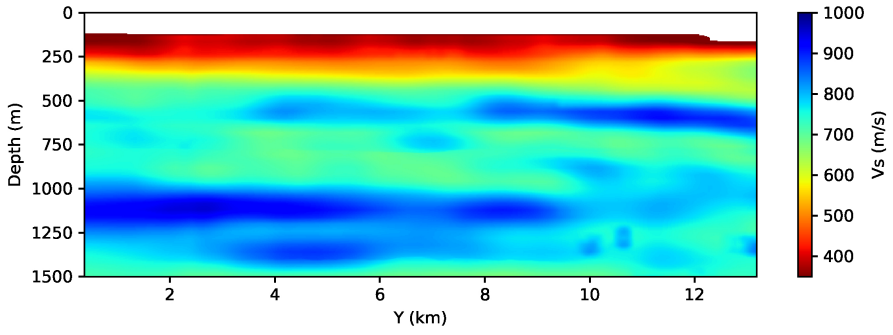

Figure 17. Shear-wave velocity Vs model from reflection tomography obtained using active source seismic data. The white top layer represents the water layer which has zero shear velocity.

that these structures are probably related to the similar structures in the phase velocity maps and might indicate useful information about the subsurface, or may be caused by poor quality data at longer periods. Similarly to the 2D results, we have low uncertainties from the surface down to 800 m (Figure 16c). Therefore, by including lateral spatial correlations in the 2D and 3D inversions, we can have greater confidence at larger depths than in the 1D inversion. Compared to the 2D uncertainty result, the 3D result shows lower uncertainties between 400 m and 800 m (Figure 16b and c), and they are also spatially smoother. This difference might be caused by errors introduced in the phase velocity maps in the initial 2D Eikonal tomography step (Zhang et al., 2018) since this produces the data used in the 2D McMC inversion. Due to the fact that surface waves are mainly sensitive to the near surface structure, small errors in the phase velocity maps will affect the deeper structure more than the shallow structure – it might be that large velocity variations at greater depths are needed to fit biased data. This may also be the reason why the results of 2D and 3D inversions show different results at depth: since the 3D inversion uses the phase velocity travel time picks directly, it naturally avoids any errors in the phase velocity maps (Zhang et al., 2018). Note that the two sides of the cross-section have higher uncertainties which is caused by lower ray path coverage at the two sides (Figure 15b).

To further validate our results and to better understand the three methods, we compare the results with the shear-wave velocity model in Figure 17 which was derived from PP-PS simultaneous joint tomography using active source seismic data (Bullock et al., 2015). Overall, the PP-PS tomography model is smoother compared to those from ambient noise dispersion inversions, which might be caused by regularization in the PP-PS tomography (which is not added explicitly in the McMC inversion). In the near surface (< 400 m), the PP-PS tomography model is very similar to the results from 2D and 3D inversions which again suggests that including lateral spatial correlations in the inversion solution improves results. Between 400 and 800 m the PP-PS tomography model shows a high velocity layer around 500 m, which cannot be observed in any of the three models from surface wave dispersion inversion. This is probably because that the frequency content of the two inversion are very different and small scale anomalies present in the PP-PS tomography are unlikely to be resolvable by Scholte wave data. Below 800 m, the PP-PS tomography model is much smoother and does not show the relatively complicated structures of the 2D and 3D results. However even though we have limited res-

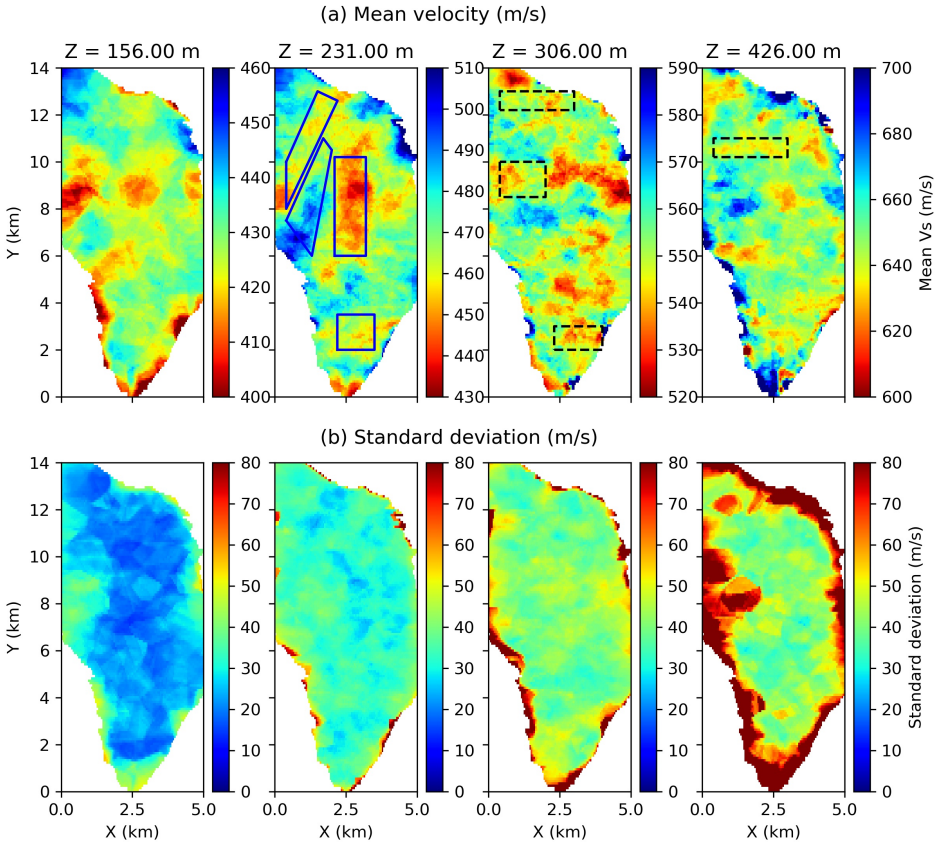

Figure 18. Horizontal slices of **(a)** the mean and **(b)** standard deviation of the shear velocity model from 3D Monte Carlo inversion at depths of 156 m, 231 m, 306 m and 426 m from left to right across the figure.

olution below 800 m, there still seems to be some similarities in the PP-PS tomography model and the 3D results, e.g. higher velocities below 1000 m and relatively smoother structure compared to the 1D and 2D results. In conclusion, the 3D inversion seems to produce a shear-velocity model that is more consistent with PP-PS tomography than do 1D and 2D inversions. Note also that the frequency range used in this study is limited to 0.7-2.0 Hz, and we only used fundamental mode surface waves. If we use a larger frequency range and include higher mode data, the results may be improved further.

Figure 18 shows horizontal slices of the pointwise mean and standard deviation of the 3D shear velocity model estimated using the 3D Monte Carlo method at depths of 156 m, 231 m, 306 m and 426 m. The blue line boxes denote the locations of features

in the fundamental mode phase velocity maps discussed above, and the black dashed-line boxes show the locations of features discussed about the phase velocity maps of the first overtone. In the near surface (< 250 m) the shear velocity model has similar structures to those in the fundamental mode phase velocity maps at short periods, for example the central low velocity anomaly which might be caused by near surface fluids and the low velocity anomaly in the south. This suggests that the phase velocities at short periods are mostly determined by the near surface structure. Due to possible interpolation errors in the Eikonal tomography step, the edges of phase velocity maps are not as well determined as in the shear velocity model, which is probably the reason why the low velocity anomaly and the high velocity anomaly in the northwest are extended in the shear velocity model compared to the phase velocity maps. In the deeper part (> 250 m), as in the phase velocity maps at longer periods, the velocity structures are more complicated than in the shallow part. However, although the phase velocity maps of the fundamental mode and the first overtone show completely different structures, the shear-velocity model inverted using only the fundamental mode indicates some similar features as observed in the first overtone phase velocity maps (black dashed-line boxes in Figure 18). For example, at the depth of 306 m there is a low velocity anomaly at the western edge between Y=8 km and Y= 10 km and a low velocity anomaly at the south around Y=2 km which also appear in the first overtone phase velocity maps. The low velocity channel existing in the first overtone phase velocity maps (red line box in Figure 9) can also be clearly observed at a depth of 426 m in the shear-velocity model. This further suggests that the complicated features in the phase velocity maps at longer periods could provide useful information about the subsurface.

At the depth of 306 m there is a low velocity channel feature between Y=3.5 km and Y=7.5km (black box in Figure 19). This channel-like feature indicates the presence of a possible palaeoriver channel at the seabed. Note that this feature cannot be observed in either fundamental mode or first overtone phase velocity maps. This suggests that the feature might be averaged out in phase velocity maps since phase velocities are a consequence of structures over a range of depths, a process that our inversion procedures are designed to undo.

Overall the standard deviation maps suggest relatively low uncertainties (< 50 m/s) at all depths, and uncertainties generally increase with depth due to the fact that surface waves have lower sensitivities at greater depth. The standard deviation map at the

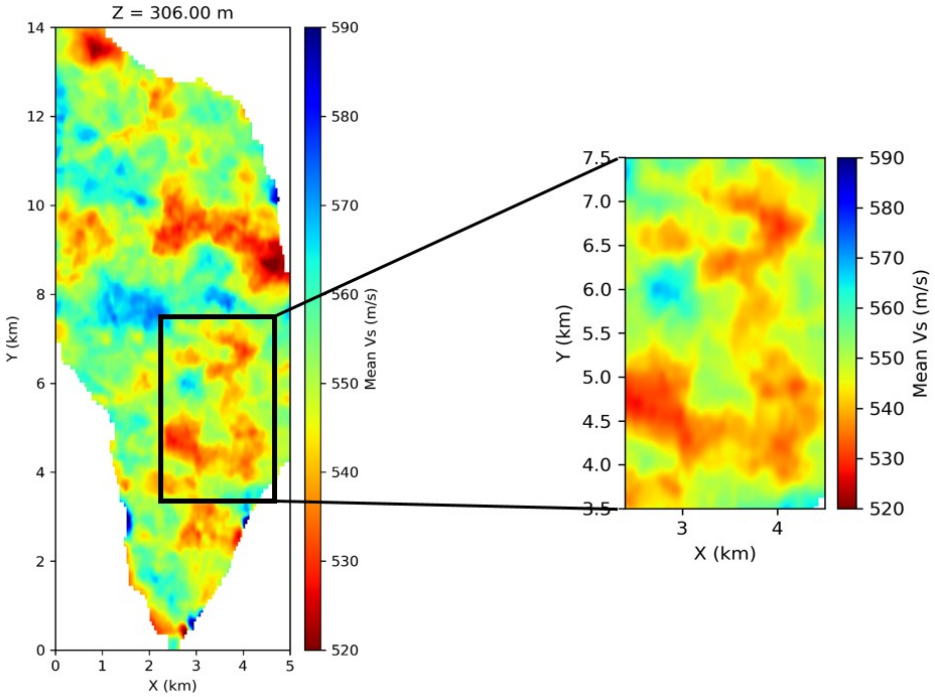

Figure 19. The Horizontal slice at depth of 306 m with a detailed structure highlighted in the magnified plot.

depth of 231 m shows relatively lower uncertainties at the locations of the velocity anomalies outlined by blue boxes, suggesting that these features are well determined. However, due to the insufficient data coverage at the edges, there is a relatively higher uncertainty area at the western edge around Y=8 km at the depth of 156 m associated with a low velocity anomaly. Similarly, at the western edge between Y=8 km and Y= 10 km the standard deviation map at a depth of 426 m shows high uncertainties.

5.4 Analysis of noise level

In this study the data noise level is estimated within the McMC method. Tomographic results are generally sensitive to the noise level as it directly affects the complexity of the model that is needed to fit the data adequately (Bodin et al., 2012). Figure 20 shows examples of the data noise level at periods of 0.7 s, 1.0 s, 1.3 s and 1.6 s estimated using the three inversion methods. Figure 20a, b show the noise distribution of all of the local phase velocities estimated using the mean scaling factor for the 1D and 2D inversion respectively, and Figure 20c shows the noise distribution of all of the used

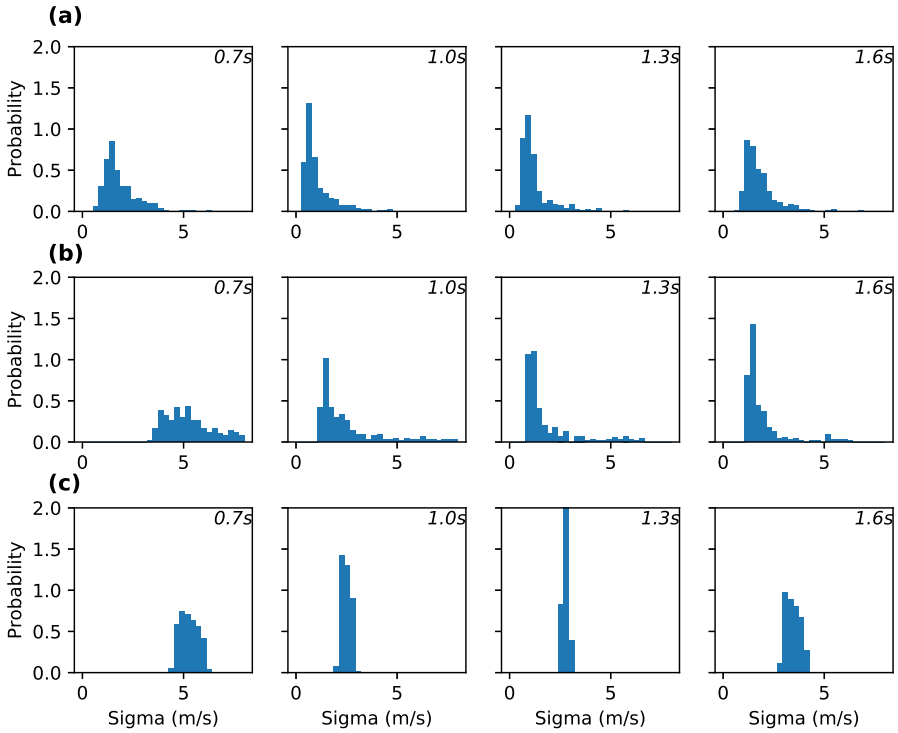

Figure 20. Noise distribution of phase velocities from the **(a)** 1D, **(b)** 2D and **(c)** 3D inversions. For each case the distribution is shown at periods of 0.7 s, 1.0 s, 1.3 s and 1.6 s from left to right.

phase velocities in the 3D inversion estimated using the mean hyperparameters. Note that the noise estimated in the 3D inversion is different from those in the 1D and 2D inversion – the 3D inversion estimates the noise level of travel times between each source-receiver pair; this is transformed to noise on velocities using straight-ray source-to-receiver distances. Overall the noise level from the three methods are relatively consistent with each other – all of them are around 2 to 4 m/s. The noise levels from the 3D inversion are slightly higher than those from the 1D and 2D inversion since they are essentially different quantities. The noise estimated from the 1D and 2D inversions are highly consistent, except at the shortest period of 0.7 s. However, from the Eikonal tomography we observed that the phase velocity map at 0.7 s itself has higher uncertainties than the others. Therefore it is possible that the 1D inversion overestimated the noise level since the method might also account for consistency with the prior range of models (Zhang et al., 2018).

To better understand the effects of the noise level on results, we performed the 1D inversions by fixing the noise level at that estimated using Eikonal tomography (Figure 21). Though there are still some discontinuities in the results due to the independence of each 1D inversion, this cross-section has a smoother structure than that in Figure13 and does not show the complicated and dipping structures observed previously. However, by doing this we inevitably sacrifice the resolution at greater depths. For example, below 550 m the velocity model is simply equal to the prior. Therefore, the hierarchical Bayesian inversion runs the risk of overfitting data for 1D inversions, while a fixed improper noise estimate might lose resolution (Bodin et al., 2012). In 1D inversions, the model is generally determined by data at tens of discrete frequency points, which might lead the inversion problem to be under-determined when complex models are used. As a result, the McMC result is very sensitive to the noise level since that determines the complexity of the model.

To better constrain the model, we carried out another inversion including the first overtone dispersion data (Figure 22). The noise level is fixed at the uncertainties estimated using Eikonal tomography. The mean velocity model (Figure 22a) has fewer discontinuities than the result from inversion using only the fundamental mode, and the layer boundaries are also better constrained in depth. The standard deviation model (Figure 22b) shows that the near surface layer has smaller uncertainties compared to the previous result. At deeper levels (500 - 700 m), the model is also better determined since

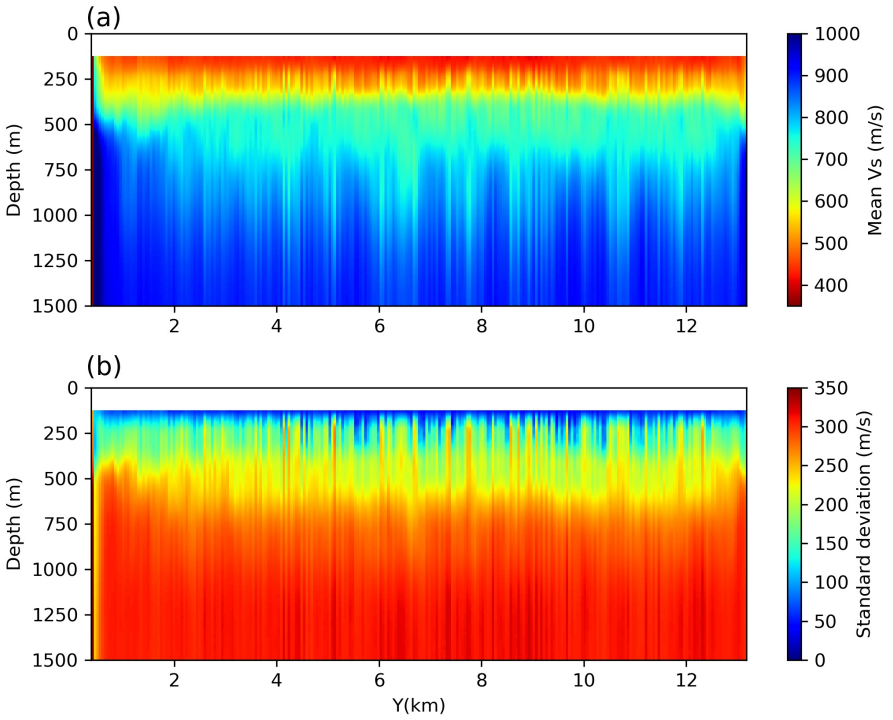

Figure 21. **(a)** Mean and **(b)** standard deviation of shear velocity Vs from independent 1D Monte Carlo inversions using only fundamental mode Rayleigh-type Scholte wave phase velocities with noise levels fixed to be uncertainties estimated from Eikonal tomography. The white top layer represents the water layer which has zero shear velocity.

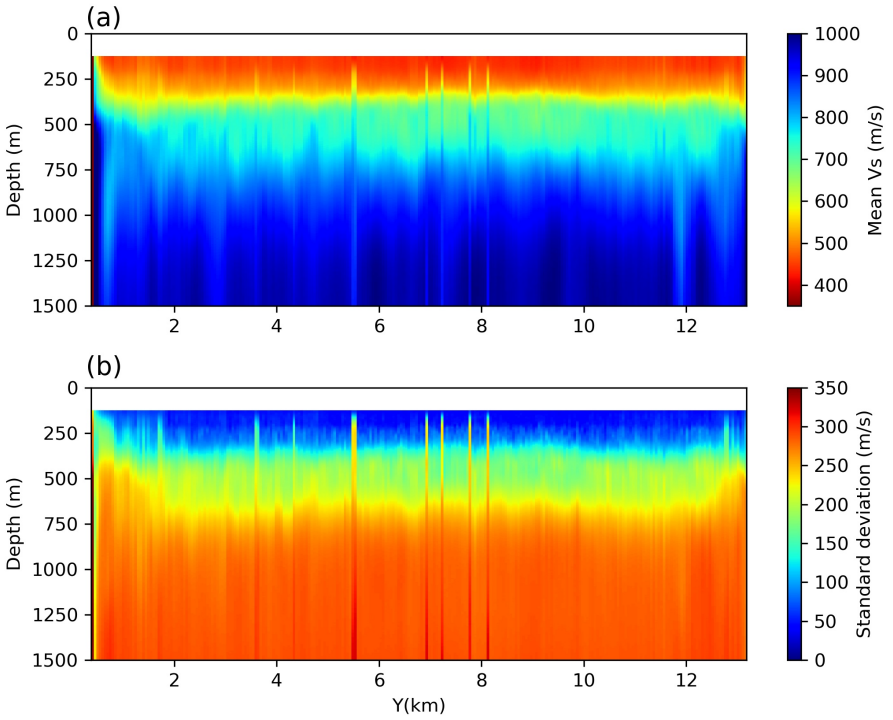

Figure 22. **(a)** Mean and **(b)** standard deviation from independent 1D Monte Carlo inversions using both the fundamental mode and the first overtone Rayleigh-type Scholte wave phase velocities, with noise levels fixed to be those uncertainties estimated from Eikonal tomography. The white top layer represents the water layer which has zero shear velocity.

it has smaller uncertainties ($\sim$ 180 m/s). However, compared to the results from 2D or 3D inversion, at greater depths (700 - 1000 m) the detailed structure that appeared in the 2D and 3D results cannot be observed and the uncertainty is also higher ($\sim$ 300 m/s), therefore we still lose some resolution.

To conclude, for 1D inversions it is possible that hierarchical Bayesian inversion can overfit the data and produce biased results. However, the noise is generally not easy to estimate and an improper noise level might also cause model resolution to be lost. By including more data (e.g. higher modes dispersion data), this issue can be partly compensated. Alternatively, we have shown that this issue can also be resolved by including lateral spatial correlations in the inversion using 2D and 3D parameterization.

6 Discussion

We observed two modes in the cross correlations of ambient noise data and used a dispersion compensation method to separate those modes. However we have shown that even after mode separation there is still some higher mode energy left in the fundamental mode estimate at low frequencies, which limits the frequency range used for tomography. Further research needs to be done in order to find methods to use the full frequency range of the data and thus to obtain more information from ambient noise cross correlations. What is more, there is a concern that the higher mode causes errors in the correlation at the fundamental mode (and vice versa) due to cross-talk in the correlation performed in our initial seismic interferometry (Halliday & Curtis, 2008). Unfortunately there is little we can do about this as mode separation in the original ambient noise remains a largely unsolved problem.

Our method of dispersion analysis needs an estimate of the phase velocity dispersion to resolve the 2π ambiguity in signal phase. This estimate can be obtained using $f-c$ analysis in our case, however it is not always possible to obtain an estimate of the phase velocity dispersion (e.g. if only a sparse array is available). In such cases some other mode separation methods based on single station measurements might be used (Trampert & Woodhouse, 1995; van Heijst & Woodhouse, 1997; Kritski et al., 2006).

We used Eikonal tomography to determine phase velocity maps by ignoring the amplitude term in equation (4). This is justified when the phase velocity map is sufficient smooth so that the spatial variation of amplitude is small (Lin et al., 2009). However,

Mordret, Shapiro, et al. (2013) have shown that this could cause some bias in phase velocity maps, especially at long periods (roughly > 1.0 s). According to their study the bias introduced by ignoring the amplitude term is, on average, about 1 m/s which is far smaller than our uncertainties. Our results therefore remain valid.

In this study, we only used the fundamental mode data when we compared the three different methods to estimate a 3D shear-velocity model. However, we have also shown that by including the first overtone dispersion data in 1D inversions, the subsurface structure can be better constrained, as has been observed previously (Gabriels et al., 1987; Xia et al., 2000, 2003). Therefore, future work will be to include those first overtone dispersion data in the 3D inversion to better constrain the subsurface structure and to further improve the resolution of greater depths.

We observed a low velocity anomaly at the center of the field both on the fundamental mode phase velocity maps at short periods (< 1.6 s) and on the shear velocity model at shallow depths (< 250 m), which is correlated with a high density region of pockmark distribution, suggesting that it might be caused by near surface fluids. Therefore, such near surface low velocity anomalies might be used as indicators of fluid leakage from the subsurface reservoirs. This suggests that ambient noise tomography might be used to monitor subsurface fluid storage reservoirs, for example in CO_2 capture and storage scenarios.

Note that in this study we did not take into account any strong anisotropy which might exist in the shallow subsurface (Barkved & Kristiansen, 2005; Barkved et al., 2005; Hatchell et al., 2009). This may introduce some bias in our final results and may explain the complicated phase velocity structures that we observed at long periods (> 1.3 s) and the complicated shear velocity structures at depth (> 250 m). However, our results should at least remain qualitatively valid, and in future it is possible to include anisotropy in 3D Monte Carlo inversions to further improve the results.

The McMC methods are generally very computationally expensive. We now compare the computational cost for the three methods used in this study. For one chain, the 1D depth inversions along the 2D section takes $\sim$186.1 cpu hours while the 2D inversion needs $\sim$206.8 cpu hours; 3D inversion costs $\sim$4824.3 cpu hours for one chain (but of course this produces a complete 3D velocity model across the entire area). Thus the 1D and 2D inversions require almost the same cpu hours which makes sense since they are es-

sentially the same apart from the different parameterization. Note that the 1D inversion and the 2D inversion are performed only along one vertical section. If we assume that we conduct the 1D inversion and the 2D inversion along all vertical sections in the 3D grid, (i.e. across all 100 cross-sections included in the grid used in Eikonal tomography), the cpu hours they consumed would be ∼18,610 cpu hours and 20,680 cpu hours respectively – significantly more than for the 3D inversion. However, the computational cost in each case strongly depends on the methods used to assess convergence, which in turn depend on subjective choices. This therefore introduces some subjectivity to the comparison. However, in our experience it is at least true that the cost of the 3D inversion is comparable to that of the 1D or 2D inversions, which has also been shown by Zhang et al. (2018). To provide an overall idea of the computational cost needed for 3D inversion, the 3D inversion herein takes approximately 22 days with each chain running on 9 CPU cores, so for all 24 chains it requires 216 CPU cores.

Note that in the 3D inversion we used an approximation forward modelling method which involves a 1D modal approximation and a 2D fast marching method. Although the method improves the accuracy of the results, the use of 1D forward modelling and 3D parametrization could fail to accurately capture the underlying properties and structures. For example, D. Yang and Oldenburg (2012) showed that 1D inversion can cause artefacts in the final results compared to a 3D inversion when using airborne time-domain electromagnetic data. Thus, in the future we hope to use a more accurate forward modelling method.

7 Conclusion

We cross correlated about 6.5 hours of ambient noise data from the Grane field, North sea and observed two modes in the constructed seabed Scholte waves. The fundamental mode dominates the signal in the cross correlations of vertical component displacement data while the first overtone dominates in the cross correlations of hydrophone components. We used a dispersion compensation method to separate the fundamental mode and the first overtone. For each mode, we determined phase velocity maps at different periods using the Eikonal tomography method. The fundamental mode phase velocity maps show a low velocity anomaly at the center of the area at short periods ($<$ 1.6 s), which might be caused by near surface fluids. At longer periods both modes show

complicated phase velocity structures, suggesting that the Grane field might have a complicated geological subsurface.

We then applied three different methods, 1D, 2D and 3D Monte Carlo inversions, to obtain shear wave velocity models of the subsurface using dispersion data of the fundamental mode as data and compared the results. The 1D results show complicated structures at deeper depths (> 250 m) which are probably caused by the independence of individual 1D inversions since the discontinuous structures do not appear in the 2D and 3D results. By including the lateral spatial correlations in the 2D and 3D inversions, we may estimate a more realistic model. The 2D inversion and the 3D inversion show lower uncertainties at greater depths (500 - 750 m), which suggests that the 2D and 3D inversion allow greater confidence at larger depths than the 1D inversion. The 3D inversion results better match a model obtained from reflection tomography than do the results from 2D or 1D inversions. This is probably due to the fact that the 3D inversion uses the measured source-to-receiver travel times directly, and therefore naturally avoids possible errors introduced in the initial (Eikonal) phase velocity tomography step required by the other methods. Though the 3D velocity model is determined using only the fundamental mode dispersion data, it shows some similar features to those which appear in the phase velocity maps of the first overtone. This provides a validation of our 3D results and may suggest that the complex phase velocity maps at longer periods could provide some useful information of the subsurface structure. Overall, the 3D McMC method provides an accurate way to study the subsurface structure using surface wave dispersion data and it is also roughly as computationally efficient as similar 1D and 2D two-step McMC inversions.

Acknowledgments

The authors would like to thank the Grane license partners Equinor ASA, Petoro AS, ExxonMobil E&P Norway AS, and ConocoPhillips Skandinavia AS for allowing us to publish this work. The views and opinions expressed in this paper are those of the authors and are not necessarily shared by the license partners. The authors thank the Edinburgh Interferometry Project sponsors (Schlumberger, Equinor and Total) for supporting this research. This work used the Cirrus UK National Tier-2 HPC Service at EPCC (http://www.cirrus.ac.uk). The dispersion curve data used in this study are available at Edinburgh DataShare (https://datashare.is.ed.ac.uk/handle/10283/3398). The raw

data may be requested from the Grane license partners Equinor ASA, Petoro As, Exxon-Mobil E&P Norway AS, and ConocoPhillips Skandinavia AS.

References

Aki, K., & Richards, P. G. (1980). *Quantitative seismology.*

Alleyne, D., Pialucha, T., & Cawley, P. (1993). A signal regeneration technique for long-range propagation of dispersive lamb waves. *Ultrasonics*, *31*(3), 201–204.

Allmark, C., Curtis, A., Galetti, E., & de Ridder, S. (2018). Seismic attenuation from ambient noise across the North Sea Ekofisk permanent array. *Journal of Geophysical Research: Solid Earth*.

Barkved, O. I., & Kristiansen, T. (2005). Seismic time-lapse effects and stress changes: Examples from a compacting reservoir. *The Leading Edge*, *24*(12), 1244–1248.

Barkved, O. I., Kristiansen, T., & Fjær, E. (2005). The 4D seismic response of a compacting reservoirexamples from the Valhall field, Norway. In *Seg technical program expanded abstracts 2005* (pp. 2508–2511). Society of Exploration Geophysicists.

Behr, Y., Townend, J., Bannister, S., & Savage, M. (2010). Shear velocity structure of the Northland Peninsula, New Zealand, inferred from ambient noise correlations. *Journal of Geophysical Research: Solid Earth*, *115*(B5).

Belhadj, J., Romary, T., Gesret, A., Noble, M., & Figliuzzi, B. (2018). New parameterizations for bayesian seismic tomography. *Inverse Problems*, *34*(6), 065007.

Bensen, G., Ritzwoller, M., & Yang, Y. (2009). A 3-D shear velocity model of the crust and uppermost mantle beneath the United States from ambient seismic noise. *Geophysical Journal International*, *177*(3), 1177–1196.

Biondi, B. (1992). Solving the frequency-dependent Eikonal equation. In *Seg technical program expanded abstracts 1992* (pp. 1315–1319). Society of Exploration Geophysicists.

Bodin, T., & Sambridge, M. (2009). Seismic tomography with the reversible jump algorithm. *Geophysical Journal International*, *178*(3), 1411–1436.

Bodin, T., Sambridge, M., Tkalčić, H., Arroucau, P., Gallagher, K., & Rawlinson, N. (2012). Transdimensional inversion of receiver functions and surface wave dispersion. *Journal of Geophysical Research: Solid Earth*, *117*(B2).

Brocher, T. M. (2005). Empirical relations between elastic wavespeeds and density in the earth's crust. *Bulletin of the seismological Society of America*, *95*(6), 2081–2092.

Bullock, A., Bekhtin, Y., Ortin, M., Mathewson, J., Henneberg, K., & Sæbø, A. (2015). Improved imaging with PP-PS simultaneous joint tomography over the Grane field. In *Seg technical program expanded abstracts 2015* (pp. 2094–2097). Society of Exploration Geophysicists.

Burdick, S., & Lekić, V. (2017). Velocity variations and uncertainty from transdimensional p-wave tomography of North America. *Geophysical Journal International*, *209*(2), 1337–1351.

Calderhead, B., & Girolami, M. (2009). Estimating Bayes factors via thermodynamic integration and population MCMC. *Computational Statistics & Data Analysis*, *53*(12), 4028–4045.

Campillo, M., & Paul, A. (2003). Long-range correlations in the diffuse seismic coda. *Science*, *299*(5606), 547–549.

Castagna, J. P., Batzle, M. L., & Eastwood, R. L. (1985). Relationships between compressional-wave and shear-wave velocities in clastic silicate rocks. *Geophysics*, *50*(4), 571–581.

Chen, X. (1993). A systematic and efficient method of computing normal modes for multilayered half-space. *Geophysical Journal International*, *115*(2), 391–409.

Chmiel, M., Mordret, A., Boué, P., Brenguier, F., Lecocq, T., Courbis, R., ... Van der Veen, W. (2019). Ambient noise multimode rayleigh and love wave tomography to determine the shear velocity structure above the groningen gas field. *Geophysical Journal International*, *218*(3), 1781–1795.

Cole, S. P. (1995). *Passive seismic and drill-bit experiments using 2-D arrays* (No. 86). Stanford University.

Crampin, S., & Båth, M. (1965). Higher modes of seismic surface waves: mode separation. *Geophysical Journal International*, *10*(1), 81–92.

Curtis, A., Gerstoft, P., Sato, H., Snieder, R., & Wapenaar, K. (2006). Seismic interferometry – turning noise into signal. *The Leading Edge*, *25*(9), 1082–1092.

Curtis, A., & Halliday, D. (2010). Directional balancing for seismic and general wavefield interferometry. *Geophysics*, *75*(1), SA1–SA14.

Curtis, A., Trampert, J., Snieder, R., & Dost, B. (1998). Eurasian fundamental

mode surface wave phase velocities and their relationship with tectonic structures. *Journal of Geophysical Research: Solid Earth*, *103*(B11), 26919–26947.

de Ridder, S., & Biondi, B. (2013). Daily reservoir-scale subsurface monitoring using ambient seismic noise. *Geophysical Research Letters*, *40*(12), 2969–2974.

de Ridder, S., Biondi, B., & Clapp, R. (2014). Time-lapse seismic noise correlation tomography at Valhall. *Geophysical Research Letters*, *41*(17), 6116–6122.

de Ridder, S., Biondi, B., & Nichols, D. (2015). Elliptical-anisotropic Eikonal phase velocity tomography. *Geophysical Research Letters*, *42*(3), 758–764.

de Ridder, S., & Dellinger, J. (2011). Ambient seismic noise Eikonal tomography for near-surface imaging at Valhall. *The Leading Edge*, *30*(5), 506–512.

Dettmer, J., & Dosso, S. E. (2012). Trans-dimensional matched-field geoacoustic inversion with hierarchical error models and interacting Markov chains. *The Journal of the Acoustical Society of America*, *132*(4), 2239–2250.

Dettmer, J., Hawkins, R., Cummins, P. R., Hossen, J., Sambridge, M., Hino, R., & Inazu, D. (2016). Tsunami source uncertainty estimation: The 2011 japan tsunami. *Journal of Geophysical Research: Solid Earth*, *121*(6), 4483–4505.

Dosso, S. E., Dettmer, J., Steininger, G., & Holland, C. W. (2014). Efficient trans-dimensional Bayesian inversion for geoacoustic profile estimation. *Inverse Problems*, *30*(11), 114018.

Dosso, S. E., Holland, C. W., & Sambridge, M. (2012). Parallel tempering for strongly nonlinear geoacoustic inversion. *The Journal of the Acoustical Society of America*, *132*(5), 3030–3040.

Dziewonski, A., Bloch, S., & Landisman, M. (1969). A technique for the analysis of transient seismic signals. *Bulletin of the seismological Society of America*, *59*(1), 427–444.

Earl, D. J., & Deem, M. W. (2005). Parallel tempering: Theory, applications, and new perspectives. *Physical Chemistry Chemical Physics*, *7*(23), 3910–3916.

Ekström, G. (2011). A global model of Love and Rayleigh surface wave dispersion and anisotropy, 25-250 s. *Geophysical Journal International*, *187*(3), 1668–1686.

Fang, H., Yao, H., Zhang, H., Huang, Y.-C., & van der Hilst, R. D. (2015). Direct inversion of surface wave dispersion for three-dimensional shallow crustal structure based on ray tracing: methodology and application. *Geophysical Journal*

International, *201*(3), 1251–1263.

Ferreira, A., Woodhouse, J., Visser, K., & Trampert, J. (2010). On the robustness of global radially anisotropic surface wave tomography. *Journal of Geophysical Research: Solid Earth*, *115*(B4).

Fink, M. (1992). Time reversal of ultrasonic fields. i. basic principles. *IEEE transactions on ultrasonics, ferroelectrics, and frequency control*, *39*(5), 555–566.

Gabriels, P., Snieder, R., & Nolet, G. (1987). In situ measurements of shear-wave velocity in sediments with higher-mode Rayleigh waves. *Geophysical prospecting*, *35*(2), 187–196.

Galetti, E., & Curtis, A. (2018). Transdimensional electrical resistivity tomography. *Journal of Geophysical Research: Solid Earth*, *123*(8), 6347–6377.

Galetti, E., Curtis, A., Baptie, B., Jenkins, D., & Nicolson, H. (2017). Transdimensional Love-wave tomography of the British Isles and shear-velocity structure of the east Irish Sea Basin from ambient-noise interferometry. *Geophysical Journal International*, *208*(1), 36–58.

Galetti, E., Curtis, A., Meles, G. A., & Baptie, B. (2015). Uncertainty loops in travel-time tomography from nonlinear wave physics. *Physical review letters*, *114*(14), 148501.

Geyer, C. J. (1994). Estimating normalizing constants and reweighting mixtures. *Technical Report*.

Green, P. J. (1995). Reversible jump Markov chain Monte Carlo computation and Bayesian model determination. *Biometrika*, 711–732.

Green, P. J., & Hastie, D. I. (2009). Reversible jump MCMC. *Genetics*, *155*(3), 1391–1403.

Halliday, D., & Curtis, A. (2008). Seismic interferometry, surface waves and source distribution. *Geophysical Journal International*, *175*(3), 1067–1087.

Hastings, W. K. (1970). Monte Carlo sampling methods using Markov chains and their applications. *Biometrika*, *57*(1), 97–109.

Hatchell, P., Wills, P., & Didraga, C. (2009). Production induced effects on near-surface wave velocities at Valhall. In *71st eage conference and exhibition incorporating spe europec 2009.*

Hawkins, R., Bodin, T., Sambridge, M., Choblet, G., & Husson, L. (2019). Trans-dimensional surface reconstruction with different classes of parameterization.

Geochemistry, Geophysics, Geosystems, *20*(1), 505–529.

Hawkins, R., & Sambridge, M. (2015). Geophysical imaging using trans-dimensional trees. *Geophysical Journal International*, *203*(2), 972–1000.

Herrin, E., & Goforth, T. (1977). Phase-matched filters: application to the study of Rayleigh waves. *Bulletin of the Seismological Society of America*, *67*(5), 1259–1275.

Herrmann, R. B. (2013). Computer programs in seismology: An evolving tool for instruction and research. *Seismological Research Letters*, *84*(6), 1081–1088.

Ing, R. K., & Fink, M. (1998). Time-reversed lamb waves. *IEEE transactions on ultrasonics, ferroelectrics, and frequency control*, *45*(4), 1032–1043.

Jan van Heijst, H., & Woodhouse, J. (1999). Global high-resolution phase velocity distributions of overtone and fundamental-mode surface waves determined by mode branch stripping. *Geophysical Journal International*, *137*(3), 601–620.

Khan, A., Zunino, A., & Deschamps, F. (2013). Upper mantle compositional variations and discontinuity topography imaged beneath Australia from Bayesian inversion of surface-wave phase velocities and thermochemical modeling. *Journal of Geophysical Research: Solid Earth*, *118*(10), 5285–5306.

Kritski, A., Vincent, A., Yuen, D., & Carlsen, T. (2006). Adaptive wavelets for analyzing dispersive seismic waves. *Geophysics*, *72*(1), V1–V11.

Kuttig, H., Niethammer, M., Hurlebaus, S., & Jacobs, L. J. (2006). Model-based analysis of dispersion curves using chirplets. *The Journal of the Acoustical Society of America*, *119*(4), 2122–2130.

Kvenvolden, K. A. (1989). Seabed pockmarks and seepages: Impact on geology, biology and the marine environment. *Science*, *244*(4904), 590–592.

Levshin, A., Ratnikova, L., & Berger, J. (1992). Peculiarities of surface-wave propagation across central Eurasia. *Bulletin of the Seismological Society of America*, *82*(6), 2464–2493.

Levshin, A., & Ritzwoller, M. (2001). Automated detection, extraction, and measurement of regional surface waves. In *Monitoring the comprehensive nuclear-test-ban treaty: Surface waves* (pp. 1531–1545). Springer.

Levshin, A. L., Pisarenko, V., & Pogrebinsky, G. (1972). On a frequency-time analysis of oscillations. In *Annales de geophysique* (Vol. 28, pp. 211–218).

Lin, F.-C., Moschetti, M. P., & Ritzwoller, M. H. (2008). Surface wave tomogra-

phy of the western United States from ambient seismic noise: Rayleigh and Love wave phase velocity maps. *Geophysical Journal International*, *173*(1), 281–298.

Lin, F.-C., Ritzwoller, M. H., & Snieder, R. (2009). Eikonal tomography: surface wave tomography by phase front tracking across a regional broad-band seismic array. *Geophysical Journal International*, *177*(3), 1091–1110.

Lin, F.-C., Ritzwoller, M. H., Townend, J., Bannister, S., & Savage, M. K. (2007). Ambient noise Rayleigh wave tomography of New Zealand. *Geophysical Journal International*, *170*(2), 649–666.

Malinverno, A. (2002). Parsimonious Bayesian Markov chain Monte Carlo inversion in a nonlinear geophysical problem. *Geophysical Journal International*, *151*(3), 675–688.

Malinverno, A., & Briggs, V. A. (2004). Expanded uncertainty quantification in inverse problems: Hierarchical Bayes and empirical Bayes. *Geophysics*, *69*(4), 1005–1016.

Malinverno, A., Leaney, S., et al. (2000). A Monte Carlo method to quantify uncertainty in the inversion of zero-offset VSP data. In *2000 seg annual meeting.*

Meier, U., Curtis, A., & Trampert, J. (2007a). A global crustal model constrained by nonlinearised inversion of fundamental mode surface waves. *Geophysical Research Letters*, *34*, L16304.

Meier, U., Curtis, A., & Trampert, J. (2007b). Global crustal thickness from neural network inversion of surface wave data. *Geophysical Journal International*, *169*(2), 706–722.

Metropolis, N., & Ulam, S. (1949). The Monte Carlo method. *Journal of the American statistical association*, *44*(247), 335–341.

Mordret, A., Landès, M., Shapiro, N., Singh, S., & Roux, P. (2014). Ambient noise surface wave tomography to determine the shallow shear velocity structure at Valhall: depth inversion with a neighbourhood algorithm. *Geophysical Journal International*, *198*(3), 1514–1525.

Mordret, A., Landès, M., Shapiro, N., Singh, S., Roux, P., & Barkved, O. (2013). Near-surface study at the Valhall oil field from ambient noise surface wave tomography. *Geophysical Journal International*, *193*(3), 1627–1643.

Mordret, A., Shapiro, N. M., & Singh, S. (2014). Seismic noise-based time-lapse

monitoring of the Valhall overburden. *Geophysical Research Letters*, *41*(14), 4945–4952.

Mordret, A., Shapiro, N. M., Singh, S. S., Roux, P., & Barkved, O. I. (2013). Helmholtz tomography of ambient noise surface wave data to estimate Scholte wave phase velocity at Valhall life of the fieldnoise tomography at Valhall. *Geophysics*, *78*(2), WA99–WA109.

Mosegaard, K., & Tarantola, A. (1995). Monte Carlo sampling of solutions to inverse problems. *Journal of Geophysical Research: Solid Earth*, *100*(B7), 12431–12447.

Nakanishi, I., & Anderson, D. L. (1983). Measurement of mantle wave velocities and inversion for lateral heterogeneity and anisotropy: 1. analysis of great circle phase velocities. *Journal of Geophysical Research: Solid Earth*, *88*(B12), 10267–10283.

Nicolson, H., Curtis, A., & Baptie, B. (2014). Rayleigh wave tomography of the British Isles from ambient seismic noise. *Geophysical Journal International*, *198*(2), 637–655.

Nicolson, H., Curtis, A., Baptie, B., & Galetti, E. (2012). Seismic interferometry and ambient noise tomography in the British Isles. *Proceedings of the Geologists' Association*, *123*(1), 74–86.

Park, C. B., Miller, R. D., & Xia, J. (1999). Multichannel analysis of surface waves. *Geophysics*, *64*(3), 800–808.

Park, C. B., Miller, R. D., Xia, J., Hunter, J. A., & Harris, J. B. (1999). Higher mode observation by the MASW method. In *Seg technical program expanded abstracts 1999* (pp. 524–527). Society of Exploration Geophysicists.

Piana Agostinetti, N., Giacomuzzi, G., & Malinverno, A. (2015). Local three-dimensional earthquake tomography by trans-dimensional Monte Carlo sampling. *Geophysical Journal International*, *201*(3), 1598–1617.

Pragt, J., Herberg, W., Meister, M., Clemmensen, C. C., Grindhaug, G., Hanken, K. J., et al. (2012). Reaming on demand-selective activation of an integrated under reamer at the Grane field in the North Sea. In *Spe deepwater drilling and completions conference.*

Rawlinson, N., Fichtner, A., Sambridge, M., & Young, M. K. (2014). Seismic tomography and the assessment of uncertainty. In *Advances in geophysics* (Vol. 55,

pp. 1–76). Elsevier.

Rawlinson, N., & Sambridge, M. (2004). Multiple reflection and transmission phases in complex layered media using a multistage fast marching method. *Geophysics*, *69*(5), 1338–1350.

Ray, A., Kaplan, S., Washbourne, J., & Albertin, U. (2017). Low frequency full waveform seismic inversion within a tree based Bayesian framework. *Geophysical Journal International*, *212*(1), 522–542.

Reiter, D. T., & Rodi, W. L. (2008). *A new regional 3-D velocity model for Asia from the joint inversion of p-wave travel times and surface-wave dispersion data* (Tech. Rep.). WESTON GEOPHYSICAL LEXINGTON MA.

Ritzwoller, M. H., & Levshin, A. L. (1998). Eurasian surface wave tomography: Group velocities. *Journal of Geophysical Research: Solid Earth*, *103*(B3), 4839–4878.

Ritzwoller, M. H., Shapiro, N. M., Barmin, M. P., & Levshin, A. L. (2002). Global surface wave diffraction tomography. *Journal of Geophysical Research: Solid Earth*, *107*(B12).

Rost, S., & Thomas, C. (2002). Array seismology: Methods and applications. *Reviews of geophysics*, *40*(3), 2–1.

Russell, D. R., Herrmann, R. B., & Hwang, H.-J. (1988). Application of frequency variable filters to surface-wave amplitude analysis. *Bulletin of the Seismological Society of America*, *78*(1), 339–354.

Saito, M. (1988). DISPER80: A subroutine package for the calculation of seismic normal-mode solutions. *Seismological algorithms*, 293–319.

Sambridge, M. (2013). A parallel tempering algorithm for probabilistic sampling and multimodal optimization. *Geophysical Journal International*, ggt342.

Savage, M. K., Lin, F.-C., & Townend, J. (2013). Ambient noise cross-correlation observations of fundamental and higher-mode rayleigh wave propagation governed by basement resonance. *Geophysical Research Letters*, *40*(14), 3556–3561.

Saygin, E., Cummins, P., Cipta, A., Hawkins, R., Pandhu, R., Murjaya, J., ... Kennett, B. (2015). Imaging architecture of the Jakarta Basin, Indonesia with transdimensional inversion of seismic noise. *Geophysical Journal International*, *204*(2), 918–931.

Sengupta, B., Friston, K. J., & Penny, W. D. (2015). Gradient-free MCMC methods for dynamic causal modelling. *NeuroImage*, *112*, 375–381.

Shapiro, N., & Ritzwoller, M. (2002). Monte-Carlo inversion for a global shear-velocity model of the crust and upper mantle. *Geophysical Journal International*, *151*(1), 88–105.

Shapiro, N. M., & Campillo, M. (2004). Emergence of broadband Rayleigh waves from correlations of the ambient seismic noise. *Geophysical Research Letters*, *31*(7).

Shapiro, N. M., Campillo, M., Stehly, L., & Ritzwoller, M. H. (2005). High-resolution surface-wave tomography from ambient seismic noise. *Science*, *307*(5715), 1615–1618.

Shearer, P. (1999). *Introduction to seismology*. Cambridge University Press.

Shen, W., Ritzwoller, M. H., & Schulte-Pelkum, V. (2013). A 3-D model of the crust and uppermost mantle beneath the central and western US by joint inversion of receiver functions and surface wave dispersion. *Journal of Geophysical Research: Solid Earth*, *118*(1), 262–276.

Shen, W., Ritzwoller, M. H., Schulte-Pelkum, V., & Lin, F.-C. (2012). Joint inversion of surface wave dispersion and receiver functions: a Bayesian Monte-Carlo approach. *Geophysical Journal International*, *192*(2), 807–836.

Simons, F. J., Van Der Hilst, R. D., Montagner, J.-P., & Zielhuis, A. (2002). Multimode Rayleigh wave inversion for heterogeneity and azimuthal anisotropy of the Australian upper mantle. *Geophysical Journal International*, *151*(3), 738–754.

Sivia, D. (1996). Data analysis: A Bayesian tutorial (oxford science publications).

Snoke, J. A., & Sambridge, M. (2002). Constraints on the S wave velocity structure in a continental shield from surface wave data: Comparing linearized least squares inversion and the direct search neighbourhood algorithm. *Journal of Geophysical Research: Solid Earth*, *107*(B5).

Stevens, J. L., Adams, D. A., & Baker, G. E. (2001). *Improved surface wave detection and measurement using phase-matched filtering with a global one-degree dispersion model* (Tech. Rep.). SCIENCE APPLICATIONS INTERNATIONAL CORP SAN DIEGO CA.

Thompson, M., Andersen, M., Elde, R., Roy, S., & Skogland, S. (2015). The startup

of permanent reservoir monitoring for snorre and grane. In *77th eage conference and exhibition 2015.*

Tomar, G., Stutzmann, E., Mordret, A., Montagner, J.-P., Singh, S. C., & Shapiro, N. M. (2018). Joint inversion of the first overtone and fundamental mode for deep imaging at the valhall oil field using ambient noise. *Geophysical Journal International*, *214*(1), 122–132.

Trampert, J., & Woodhouse, J. H. (1995). Global phase velocity maps of Love and Rayleigh waves between 40 and 150 seconds. *Geophysical Journal International*, *122*(2), 675–690.

van Heijst, H. J., & Woodhouse, J. (1997). Measuring surface-wave overtone phase velocities using a mode-branch stripping technique. *Geophysical Journal International*, *131*(2), 209–230.

van Manen, D.-J., Curtis, A., & Robertsson, J. O. (2006). Interferometric modeling of wave propagation in inhomogeneous elastic media using time reversal and reciprocity. *Geophysics*, *71*(4), SI47–SI60.

van Manen, D.-J., Robertsson, J. O., & Curtis, A. (2005). Modeling of wave propagation in inhomogeneous media. *Physical Review Letters*, *94*(16), 164301.

Wapenaar, K. (2004). Retrieving the elastodynamic green's function of an arbitrary inhomogeneous medium by cross correlation. *Physical review letters*, *93*(25), 254301.

Wapenaar, K., & Fokkema, J. (2006). Greens function representations for seismic interferometry. *Geophysics*, *71*(4), SI33–SI46.

Weaver, R. L., Hadziioannou, C., Larose, E., & Campillo, M. (2011). On the precision of noise correlation interferometry. *Geophysical Journal International*, *185*(3), 1384–1392.

Webb, S. C. (1998). Broadband seismology and noise under the ocean. *Reviews of Geophysics*, *36*(1), 105–142.

Wielandt, E. (1993). Propagation and structural interpretation of non-plane waves. *Geophysical Journal International*, *113*(1), 45–53.

Wilcox, P. D. (2003). A rapid signal processing technique to remove the effect of dispersion from guided wave signals. *IEEE transactions on ultrasonics, ferroelectrics, and frequency control*, *50*(4), 419–427.

Wu, B., & Chen, X. (2016). Stable, accurate and efficient computation of normal

modes for horizontal stratified models. *Geophysical Journal International*, *206*(2), 1281–1300.

Xia, J., Miller, R. D., & Park, C. B. (2000). Advantages of calculating shear-wave velocity from surface waves with higher modes. In *Seg technical program expanded abstracts 2000* (pp. 1295–1298). Society of Exploration Geophysicists.

Xia, J., Miller, R. D., Park, C. B., & Tian, G. (2003). Inversion of high frequency surface waves with fundamental and higher modes. *Journal of Applied Geophysics*, *52*(1), 45–57.

Xu, K., Ta, D., Moilanen, P., & Wang, W. (2012). Mode separation of lamb waves based on dispersion compensation method. *The Journal of the Acoustical Society of America*, *131*(4), 2714–2722.

Yang, D., & Oldenburg, D. W. (2012). Three-dimensional inversion of airborne time-domain electromagnetic data with applications to a porphyry deposit. *Geophysics*, *77*(2), B23–B34.

Yang, Y., Ritzwoller, M. H., Levshin, A. L., & Shapiro, N. M. (2007). Ambient noise Rayleigh wave tomography across Europe. *Geophysical Journal International*, *168*(1), 259–274.

Yanovskaya, T., Levshin, A., Its, E., Lander, A., Bukchin, B., Barmin, M., & Ratnikova, L. (2012). *Seismic surface waves in a laterally inhomogeneous Earth* (Vol. 9). Springer Science & Business Media.

Yao, H., & Van Der Hilst, R. D. (2009). Analysis of ambient noise energy distribution and phase velocity bias in ambient noise tomography, with application to SE Tibet. *Geophysical Journal International*, *179*(2), 1113–1132.

Yao, H., van Der Hilst, R. D., & De Hoop, M. V. (2006). Surface-wave array tomography in SE tibet from ambient seismic noise and two-station analysis–i. phase velocity maps. *Geophysical Journal International*, *166*(2), 732–744.

Yilmaz, Ö. (2001). *Seismic data analysis* (Vol. 1). Society of exploration geophysicists.

Young, M. K., Rawlinson, N., & Bodin, T. (2013). Transdimensional inversion of ambient seismic noise for 3D shear velocity structure of the Tasmanian crust. *Geophysics*, *78*(3), WB49–WB62.

Zhang, X., Curtis, A., Galetti, E., & de Ridder, S. (2018). 3-D Monte Carlo surface wave tomography. *Geophysical Journal International*, *215*(3), 1644–1658.

1358 Zhdanov, M. S. (2002). *Geophysical inverse theory and regularization problems*
1359 (Vol. 36). Elsevier.
1360 Zheng, D., Saygin, E., Cummins, P., Ge, Z., Min, Z., Cipta, A., & Yang, R. (2017).
1361 Transdimensional Bayesian seismic ambient noise tomography across SE Tibet.
1362 *Journal of Asian Earth Sciences*, *134*, 86–93.
1363 Zielhuis, A., & Nolet, G. (1994). Deep seismic expression of an ancient plate bound-
1364 ary in Europe. *Science*, *265*(5168), 79–81.
1365 Zigone, D., Ben-Zion, Y., Campillo, M., & Roux, P. (2015). Seismic tomography of
1366 the Southern California plate boundary region from noise-based Rayleigh and
1367 Love waves. *Pure and Applied Geophysics*, *172*(5), 1007–1032.
1368 Zulfakriza, Z., Saygin, E., Cummins, P., Widiyantoro, S., Nugraha, A. D., Lühr,
1369 B.-G., & Bodin, T. (2014). Upper crustal structure of central Java, Indonesia,
1370 from transdimensional seismic ambient noise tomography. *Geophysical Journal*
1371 *International*, *197*(1), 630–635.